Geosci. Model Dev., 19, 7279–7301, 2026
https://doi.org/10.5194/gmd-19-7279-2026

Geoscientific Model Development
Open Access

Model evaluation paper

Global fully coupled climate-aerosol CMA-CPSv4 – Part 1: Aerosol simulation performance

Mengzhe Zheng[1,2,3], **Tongwen Wu**[1,3,4], **Yixiong Lu**[3], **Weihua Jie**[3], **Yiming Liu**[3], **Xiaoge Xin**[3], **Jie Zhang**[3], **He Zhao**[3], **Xindan Zhang**[3], and **Jiajie Yang**[1,3]

[1]Chinese Academy of Meteorological Sciences, China Meteorological Administration, Beijing 100081, China
[2]University of Chinese Academy of Sciences, Beijing 100049, China
[3]Earth System Modeling and Prediction Centre, China Meteorological Administration, Beijing 100081, China
[4]State Key Laboratory of Severe Weather Meteorological Science and Technology, China Meteorological Administration, Beijing 100081, China

Correspondence: Tongwen Wu (twwu@cma.gov.cn)

Received: 1 February 2026 – Discussion started: 13 March 2026
Revised: 1 June 2026 – Accepted: 27 July 2026 – Published: 6 August 2026

Abstract. This study provides a comprehensive description of the China Meteorological Administration Climate Prediction System version 4 (CMA-CPSv4), which is developed based on the fully coupled global climate-aerosol Beijing Climate Center Earth System Model (BCC-ESM1). It is updated from its previous version, CMA-CPSv3, which was based on the high-resolution Beijing Climate Center Climate System Model version 2 (BCC-CSM2-HR). In contrast to CMA-CPSv3, CMA-CPSv4 is capable of simulating the dynamic evolution of aerosols and their feedback on the climate system. This study aims to evaluate the reproducibility of atmospheric aerosols in CMA-CPSv4 under the forcing of observed atmospheric circulation. The 20-year simulations for the period 2001–2020 are conducted. The results show that CMA-CPSv4 reasonably captures the global spatial distribution and temporal variations in mass concentrations for five categories of dust, sea salt, sulfates, organic carbon, and black carbon, as well as aerosol optical depth (AOD). In East Asia, simulated fine-mode particulate matter $PM_{2.5}$ concentrations are generally consistent with the CMIP6 multi-model ensemble mean (MME), although dust concentrations over the Taklamakan–Mongolia–North China regions are slightly underestimated, and sulfate concentrations are overestimated over the oceans. In addition, several severe dust pollution events in northern China are successfully reproduced, demonstrating the capability of CMA-CPSv4 to simulate aerosol concentrations and extreme pollution events. The reasonable simulation of aerosol distribution is fundamental for studying aerosol-climate interactions and the impact of aerosols on numerical weather and climate prediction in our future work.

1 Introduction

Atmospheric aerosols influence weather and climate through direct radiative effects and indirect cloud effects (Houghton et al., 2001; Lohmann et al., 2010b; Ming et al., 2005). Aerosol particles scatter and absorb solar radiation, cooling the Earth's surface (Ångström, 1929; McCormick and Ludwig, 1967). Aerosols can also act as cloud condensation nuclei, altering cloud droplet number concentration and influencing cloud microphysical and optical properties, such as cloud albedo, cloud amount, and cloud lifetime (Twomey, 1974, 1977), and then affect precipitation efficiency (Albrecht, 1989; Rosenfeld, 2000). Additionally, precipitation generated by clouds removes aerosols from the atmosphere, thereby affecting aerosol-cloud interactions. Earth System Models (ESMs) are comprehensive models that extend the coupled atmosphere-oceans-sea ice-land surface climate system models (CSMs) to include various biogeochemical cycles, aerosol chemical and physical processes, and their feedbacks (Flato, 2011). These models are essential tools for investigating the aerosol processes and their interactions with weather and climate. Many countries, including China, have developed their own ESMs (Bathiany et al., 2010; Bodas-

Salcedo et al., 2008; Chylek et al., 2011; Dunne et al., 2020; Sellar et al., 2019; Tilmes et al., 2015; Van Noije et al., 2021; Watanabe et al., 2011; Wu et al., 2020b; Zhang et al., 2020). These models are widely applied in climate research (Asaadi et al., 2024; Friedlingstein et al., 2006, 2014; Kaufhold et al., 2025).

In recent years, there has been increasing attention on aerosol forecasting and the impact of aerosols on weather and climate prediction. A handful of centers have provided operational, near-real-time, and seasonal global aerosol forecasts. For example, the Integrated Forecasting System (IFS) operated by the European Centre for Medium-Range Weather Forecasts (ECMWF) offers near-real-time global analyses and operational five-day forecasts of atmospheric aerosols, AOD, and PM (Rémy et al., 2022). Similarly, the National Oceanic and Atmospheric Administration (NOAA)'s latest operational aerosol forecast model, GEFS-Aerosols, predicts five aerosol species (dust, sea salt, black carbon, organic carbon, and sulfate) and total AOD over a 5–7 d period. It also captures severe biomass burning events (Bhattacharjee et al., 2023). The Goddard Earth Observing System composition forecast system (GEOS-CF) and Sub-seasonal to Seasonal prediction system (GEOS-S2S) provide operational forecasts of atmospheric constituents and AOD at weather scales (within 5 d) and sub-seasonal to seasonal scales (Keller et al., 2021; Molod et al., 2020). In addition, aerosols also influence the forecast outcomes of numerical weather prediction (NWP). Huang and Ding (2021) indicated that aerosols are a crucial factor contributing to temperature forecast biases in NWP. Mulcahy et al. (2014) found that increasing the complexity of the aerosol scheme within the UK Met Office Unified Model yielded significant benefits for the model's prediction capability. Benedetti and Vitart (2018) also showed that interactive aerosols improved sub-seasonal forecasts for spring and summer on a monthly scale. However, other studies (such as Sun et al., 2025) suggested that the interactive aerosol scheme used in the simulation did not significantly improve the forecast skills for temperature at 2 m, 500 hPa potential height, and precipitation at sub-seasonal to seasonal scales. Uncertainties in aerosol emissions, modelling frameworks, and physicochemical schemes significantly influence the results of modelling and climate prediction systems (Fletcher et al., 2018; Lohmann and Ferrachat, 2010a; Wei et al., 2019).

China Meteorological Administration (CMA) has been focused on developing the fully-coupled Beijing Climate Center Climate System Model (BCC-CSM) and Beijing Climate Center Earth System Model (BCC-ESM) since 2005 (Wu et al., 2013, 2014, 2019, 2020b, 2021). The BCC-CSMs and BCC-ESMs with different resolutions have been widely employed in climate research and CMIP5 and CMIP6 (Wu et al., 2020b) and also used for operational climate predictions. The BCC-CSM2 is the second-generation high-resolution model (BCC-CSM2-HR, $\sim$45 km) and has good performance in simulating large-scale mean climate and several key phenomena, such as the Intertropical Convergence Zone (ITCZ), tropical cyclones (TCs), Madden-Julian Oscillation (MJO), and stratospheric Quasi-biennial Oscillation (QBO) (Lu et al., 2020, 2021; Wu et al., 2021; Zheng et al., 2024). Based on the high-resolution BCC-CSM2-HR, the CMA Climate Prediction System version 3 (CMA-CPSv3) was established in 2019 and has been used for operational predictions from sub-seasonal to seasonal and annual scales, providing monthly and seasonal climate forecasts (Liang et al., 2022; Liu et al., 2021; Yang et al., 2025). BCC-ESM1 is the first-generation ESM developed by CMA (Wu et al., 2020b), which participated in two CMIP6-endorsed research initiatives: the Coupled Climate-Carbon Cycle Model Intercomparison Project (C4MIP; Jones et al., 2016) and the Aerosol Chemistry Model Intercomparison Project (AerChemMIP; Collins et al., 2017). It is widely employed in climate and ecological environment research (Lu et al., 2025; Su et al., 2022; Zhang et al., 2021a; Zhou et al., 2023) and contributes to model evaluation and comparative studies (Firpo et al., 2022; Liu et al., 2022; Zhang et al., 2021b).

Recently, based on the CMA-CPSv3 and BCC-ESM1, we upgraded the prediction system CMA-CPSv3 to the CMA-CPSv4, in which atmospheric aerosols are prognostic values and treated as those in BCC-ESM1 (Wu et al., 2020b), considering their dynamic evolution and feedback on radiation, cloud and precipitation. The purpose of this study is to evaluate the aerosol simulation performance of CMA-CPSv4 under the forcing of observed meteorological fields. Aerosol feedback on climate prediction, including aerosol–radiation interactions (ARI) and aerosol–cloud interactions (ACI), will be investigated in our separate work. In Sect. 2, a simple description of the CMA-CPSv4 will be presented. The experimental design and the observational data used in this study are also described in Sect. 2. In Sect. 3, we present the assessment of the global distribution and vertical distribution of major aerosols and AOD. The simulation performance of the model for $PM_{2.5}$ in East Asia and severe dust pollution events occurring in North China is also evaluated. Section 4 summarizes the conclusions and discussions.

2 Model, experimental design, and data

2.1 Model description

CMA-CPSv3 is established based on a high-resolution version BCC-CSM2-HR fully coupled with four components (atmosphere, ocean, land, and sea ice) through fluxes of momentum, energy, and water at their interfaces (Wu et al., 2020b), and its coupled assimilation system (Liu et al., 2021). The atmospheric component in BCC-CSM2-HR is the Beijing Climate Center Atmospheric General Circulation Model version 3 (BCC-AGCM3, Wu et al., 2019), with a horizontal resolution of T266 triangular truncation (approximately 45 km) and 56 vertical hybrid sigma–pressure layers, with the top level at 0.1 hPa. The ocean component is the Modular Ocean Model Version 5 (MOM5, Griffies, 2012), with a horizontal resolution of 0.25° and 50 vertical levels. The land component is the Beijing Climate Center Atmosphere-Vegetation Interaction Model version 2 (BCC-AVIM2.0, Li et al., 2019), and the sea-ice component is the Sea Ice Simulator 5 (SIS 5, Delworth et al., 2006).

Recently, CMA-CPSv3 has been updated to CMA-CPSv4, in which the atmospheric component BCC-AGCM3 is updated to BCC-AGCM3-Chem, and the other three components (land, ocean, sea ice) in CMA-CPSv4 keep the same as those in CMA-CPSv3. BCC-AGCM3-Chem is based on the BCC-AGCM3 and coupled with interactive aerosols and their related atmospheric chemistry (here, other atmospheric chemistry predictions are not activated in order to improve computational efficiency) based on BCC-ESM1 (Wu et al., 2020b). Model physics in BCC-AGCM3-Chem has been further modified, including cloud parameterization, deep and shallow cumulus convection, boundary layer turbulence, and gravity wave schemes (Lu et al., 2020, 2021; Wu et al., 2021; Zheng et al., 2024). Those modifications are useful for improving the simulation of the Intertropical Convergence Zone (ITCZ), precipitation, tropical cyclones (TCs), the MJO, and the stratospheric QBO.

There are 13 major prognostic aerosol species involved in BCC-AGCM3-Chem, which are the same as those in BCC-ESM1 (Wu et al., 2020b), including four bins each for soil dust (DST01, DST02, DST03, DST04) and sea salt (SSLT01, SSLT02, SSLT03, SSLT04); two types of organic carbon (hydrophobic OC1 and hydrophilic OC2); two types of black carbon (hydrophobic BC1 and hydrophilic BC2) and sulfate (SO_4^{2-}). These species are interactively treated through processes including emission, transport, gas-phase chemical reactions, secondary aerosol formation, gravitational settling, dry deposition, wet scavenging by clouds and precipitation, and aerosol effects on radiation, clouds, and precipitation. In the current version, the radiative transfer parameterization of BCC-AGCM3-Chem only accounts for the direct radiative effect of these 13 prognostic aerosol species, while other aerosol species, such as nitrate and ammonium, are not included as prognostic variables.

Aerosol-cloud interactions within the CMA-CPSv4 are manifested through the modulation of liquid cloud droplet number concentration (N_{cdnc}, cm^{-3}) and effective droplet radius. The cloud droplet number concentration is parameterised using an empirical function proposed by Boucher and Lohmann (1995) and Quaas et al. (2006):

$$N_{cdnc} = \exp(5.1 + 0.41 \times \ln(m_{ss} + m_{oc} + m_{so4} + m_{NH4NO3})) \quad (1)$$

Four types of hydrophilic aerosols influence cloud droplet number concentration, including bin 1 of sea salt, hydrophilic organic carbon, sulfates, and ammonium nitrate (NH_4NO_3). Among these, NH_4NO_3 is prescribed using a monthly mean climatology derived from NCAR CAM-Chem (Lamarque et al., 2012). Further details may be referred to the description in Wu et al. (2020b). In BCC-AGCM3 of previous CMA-CPSv3, those major aerosol mass concentrations for radiative transfer parameterization and N_{cdnc} estimates are prescribed from CMIP5-recommended historical data (Taylor et al., 2012).

In CMA-CPSv4, dust emission is interactively determined through coupling between the land component BCC-AVIM2.0 and BCC-AGCM3-Chem. BCC-AVIM2.0 provides land-surface conditions, and the emission flux is computed using a saltation–sand-blasting scheme that depends on wind friction velocity, soil moisture, and vegetation or snow cover (Zender et al., 2003). Sea salt emission is calculated online and parameterized as a function of the 10 m wind speed over the sea surface (Mahowald et al., 2006). Sulfates are formed from their precursors sulfur dioxide (SO_2) through gas-phase oxidation and aqueous-phase oxidation within cloud droplets. The primary sources of SO_2 include fuel combustion, industrial activities, and volcanic eruptions. The oxidation of dimethyl sulfide (DMS) produced by oceanic phytoplankton activity is also a major source of SO_2 (Table 1). Carbonaceous aerosols, including OC and BC, are categorised as hydrophobic and hydrophilic aerosols. Hydrophobic aerosols convert at a constant rate into hydrophilic aerosols. OC and BC originate primarily from fossil fuel combustion and biomass burning. The gas-phase chemistry in CMA-CPSv4 involves the following 6 reactions, with their reaction equations and corresponding rate coefficients listed in Table 1. For the oxidants OH and NO_3, the data are prescribed based on MOZART-4 climatological data, which are derived from different treatments within the BCC-ESM1 (Wu et al., 2020b).

2.2 Experimental design

In order to validate the performance of CMA-CPSv4 in simulating aerosols, we conducted a 20-year experiment from January 2001 to December 2020. The experiment was forced by atmospheric fields including horizontal winds, temperature, and specific humidity nudged toward 6-hourly ERA5 reanalysis fields (Hersbach et al. 2020, 2023a, b), and the ocean temperature in the ocean component of CMA-CPSv4 was nudged toward an ocean reanalysis produced by a newly developed coupled assimilation system based on CMA-CPSv3 (Liu et al., 2021).

The simulations were run with prescribed forcings based on CMIP6-recommended data (https://esgf-node.llnl.gov/search/input4mips/, last access: 4 January 2025) including: (1) greenhouse gas concentrations such as CO_2, N_2O, CH_4, CFC-11, and CFC-12 with monthly zonal-mean values, and ozone concentrations with monthly gridded values; (2) annual mean total solar irradiance derived from the CMIP6 solar forcing; and (3) stratospheric aerosols from volcanic eruptions. Aerosol emissions were also taken from CMIP6-

Table 1. Gas-phase chemical reactions of bulk aerosol precursors in CMA-CPSv4 and corresponding reaction rates (s^{-1}).

Chemical reactions	Rate
$SO_2 + OH \rightarrow SO_4^{2-}$	$k_o \,/\, (1.0 + k_o \times M \,/\, k_i) \times f \times (1.0 \,/\, (1.0 + \log10(k_o \times M \,/\, k_i))$, in which $k_o = 3.0 \times 10^{-31} \times (300/T) \times 3.3$; $k_i = 1.0 \times 10^{-12}$; $f = 0.6$
$DMS + OH \rightarrow SO_2$	$9.60 \times 10^{-12} \times \exp(-234.0/T)$
$DMS + OH \rightarrow 0.5 \times SO_2 + 0.5 \times HO_2$	$1.7 \times 10^{-42} \times \exp(7810/T) \times M \times 0.21/(1 + 5.5 \times 10^{-31} \times \exp(7460/T) \times M \times 0.21)$
$DMS + NO_3 \rightarrow SO_2 + HNO_3$	$1.90 \times 10^{-13} \times \exp(520/T)$
$BC1 \rightarrow BC2$	7.10×10^{-6}
$OC1 \rightarrow OC2$	7.10×10^{-6}

Notes: T denotes the ambient temperature, units: K. M denotes gas concentration, units: molec. cm^{-3}. OH and NO_3 are prescribed based on MOZART-4 climatological data (https://www2.acom.ucar.edu/gcm/mozart-4, last access: 4 January 2025).

recommended datasets, including biomass burning emissions (Van Marle et al., 2017) and anthropogenic and open burning emissions (Feng et al., 2020; Gidden et al., 2019; Hoesly et al., 2018).

2.3 Verification data sets

The daily Modern-Era Retrospective Analysis for Research and Applications, version 2 aerosol reanalysis (MERRA-2; Buchard et al., 2017; Gelaro et al., 2017; Randles et al., 2017) and the multi-model mean of 10 Earth system models (ESMs) participating in CMIP6 (Eyring et al., 2016) are used to evaluate the CMA-CPSv4 simulation of five major aerosol species (dust, sea salt, sulfate, OC, and BC). MERRA-2 reanalysis is widely used for aerosol model evaluation (e.g., Buchard et al., 2017; Gui et al., 2026; Randles et al., 2017; Su et al., 2022; Turnock et al., 2020; Zhou et al., 2023). The CMIP6 ESMs include BCC-ESM1, CESM2-WACCM, EC-Earth3-AerChem, GFDL-ESM4, IPSL-CM5A2-INCA, MIROC-ES2L, MPI-ESM1.2-HAM, MRI-ESM2-0, NorESM2-LM, and UKESM1-0-LL. These model outputs are derived from the historical simulations of the first ensemble member (r1i1p1f1) for the period 1850–2014, obtained from the Earth System Grid Federation (ESGF, https://esgf-node.ornl.gov/search?project=input4MIPs, last access: 2 March 2025). The simulated data from 2001 to 2014 are selected and interpolated to a $1° \times 1°$ grid for evaluation. As surface $PM_{2.5}$ is not directly available from all CMIP6 models, $PM_{2.5}$ concentrations are calculated following previous studies (Su et al., 2022; Turnock et al., 2020):

$$PM_{2.5} = BC + OC + SO_4 + 0.1 \times DU + 0.25 \times SS \quad (2)$$

This approach assumes that 10 % of dust and 25 % of sea salt contribute to the $PM_{2.5}$ fraction and has been widely applied in CMIP5 and ACCMIP analyses (Silva et al., 2017; Turnock et al., 2020). In addition, two ground-based observational datasets are used to evaluate the simulated surface $PM_{2.5}$ concentrations. These include monthly mean $PM_{2.5}$ measurements from 28 stations of the East Asian Acid Deposition Monitoring Network (EANET, http://www.eanet.asia, last access: 4 March 2025, Ohizumi, 2023) and annual mean $PM_{2.5}$ concentrations from 364 urban monitoring sites operated by the China National Environmental Monitoring Centre (CNEMC, http://www.cnemc.cn, last access: 6 March 2025), and daily $PM_{2.5}$ observations from the CNEMC for the period 2014–2019. AOD observations are taken from the AErosol RObotic NETwork (AERONET, https://aeronet.gsfc.nasa.gov/new_web/, last access: 18 March 2025, Holben et al., 1998) using the cloud-screened and quality-assured Level 2.0 version 3.0 monthly product. AOD at 550 nm is derived from a log-linear interpolation between measurements at 440 and 675 nm (Dai et al., 2014; Schuster et al., 2006). In addition, monthly AOD products from the Moderate Resolution Imaging Spectroradiometer (MODIS, https://ladsweb.modaps.eosdis.nasa.gov/, last access: 20 March 2025, Platnick et al., 2017) and the Multi-angle Imaging SpectroRadiometer (MISR, https://l0dup05.larc.nasa.gov/L3Web/, last access: 20 March 2025, Diner et al., 1998) are also used for model evaluation.

The study also assesses the model's ability to reproduce monthly variations in $PM_{2.5}$ and AOD in different regions around the world according to definitions of the Hemispheric Transport of Air Pollution phase 3 (HTAP v3; Crippa et al., 2023). HTAP v3 was developed under the Task Force on Hemispheric Transport of Air Pollution (TF HTAP) as a comprehensive tool for simulating and analyzing the transboundary transport of air pollutants. In HTAP v3, the global land surface is divided into nine source regions: East Asia (EAS), the European Monitoring and Evaluation Programme domains (EMEP East Domain, EMEP_E; and EMEP West Domain, EMEP_W), Mexico/Central America/Caribbean (MCA), North America (NAM), South Asia (SAS), Southeast Asia (SEA), Southern and Eastern Mediterranean (SMD), and the Rest of the World (ROW; including South America, Southern Africa, and Australia). The regional definitions used in HTAP3-OPNS are publicly available (https://zenodo.org/records/12654038, last access: 20 March 2025, Butler, 2024).

3 Model results and evaluation

3.1 Aerosol global distributions

Figure 1 shows the global spatial distributions of annual mean column-integrated concentrations of dust, sea salt, sulfate, OC and BC aerosols, averaged for the period 2001–2020 from CMA-CPSv4 simulations. The results are compared with the MERRA-2 reanalysis for the same period and with the multi-model ensemble mean of historical simulations for 2001–2014. High dust concentrations are mainly located over arid and semi-arid regions, including the Sahara, Arabian, and Taklamakan deserts, and their downwind areas (Fig. 1a–c). These areas are collectively referred to as the "dust belt" (Ginoux et al., 2012). CMA-CPSv4 reproduces the spatial pattern of dust concentrations in this region reasonably well but exhibits regional discrepancies in dust intensity. The model underestimates dust concentrations over the Taklamakan–Mongolia–North China region while overestimating them over North Africa and the Caspian Sea. Sea salt aerosols are primarily distributed over the Southern Ocean, the tropical South Indian Ocean, and the tropical Pacific Ocean, corresponding to regions of strong near-surface winds (Fig. 1d–f). MERRA-2 exhibits systematically higher concentrations than CMIP6 MME, which may reflect known biases, including an erroneous lake-masking algorithm, weak wet deposition and excessive coastal intrusion, all of which may contribute to an overall overestimation of sea salt concentrations (Buchard et al., 2017; Provençal et al., 2017; Randles et al., 2017). In comparison, CMA-CPSv4 simulates slightly lower concentrations in these regions, with values closer to those of the CMIP6 MME. The high concentrations of anthropogenic aerosols occur in high-emission areas associated with human activities. Sulfate aerosols, produced primarily through the oxidation of SO_2, are mainly concentrated over East Asia, South Asia, Europe, and the Middle East. The CMA-CPSv4 captures the distribution features of sulfate aerosols over land but overestimates their concentrations over the oceans (Fig. 1g–i). Carbonaceous aerosols (BC and OC), mainly from biomass burning and fossil fuel combustion, are concentrated in East Asia, Southeast Asia, South Asia, Africa, and South America. The simulated BC and OC concentrations are close to those in MERRA-2 and the multi-modal ensemble mean over land (Fig. 1j–o). The global mean values of dust ($37.87\,\mathrm{mg\,m^{-2}}$) and sulfate ($3.99\,\mathrm{mg\,m^{-2}}$) simulated by CMA-CPSv4 exceed those from MERRA-2 (33.92 and $3.03\,\mathrm{mg\,m^{-2}}$, respectively) and the multi-model ensemble mean (26.86 and $3.18\,\mathrm{mg\,m^{-2}}$, respectively). Such differences likely arise from variations in dry deposition parameterizations and emission inventories (Kong et al., 2025; Pleim et al., 2022). For sea salt, OC, and BC aerosols, the simulated global means lie between the corresponding MERRA-2 and the ensemble mean values. Spatial correlations between CMA-CPSv4 and MERRA-2 are 0.93 for dust, 0.92 for sea salt, 0.84 for sulfate, 0.84 for OC, and 0.90 for BC, reflecting consistency in their large-scale spatial distributions. Overall, CMA-CPSv4 reproduces the large-scale spatial distributions of the five aerosol species, although noticeable deviations remain in the simulated dust and sulfate concentrations.

Figure 2 presents the zonal mean column mass concentrations of dust, sea salt, sulfate, OC and BC aerosols simulated by CMA-CPSv4 (red line), in comparison with the MERRA-2 reanalysis (blue line) and the CMIP6 MME (black line). Compared to MERRA-2 and MME, CMA-CPSv4 reproduces the latitudinal patterns and peak locations of dust concentrations, although it overestimates values between 15° S and 30° N (Fig. 2a). At other latitudes, simulated dust concentrations are consistent with the multi-model ensemble mean but remain lower than MERRA-2 estimates. For sea salt aerosols, CMA-CPSv4 captures the two tropical peak concentrations present in MERRA-2, while underestimating sea salt concentrations near 60° S (Fig. 2b). The model reproduces the observed sulfate maximum near 25° N but exhibits positive biases in the tropics and Southern Hemisphere (SH) (Fig. 2c). The overestimation is likely linked to high model-simulated DMS emissions from oceanic phytoplankton activity, which enhance secondary sulfate formation or inadequate removal of sulfates over the ocean in the model. For carbonaceous aerosols, the simulated OC and BC concentrations decrease from the tropics toward the poles, consistent with MERRA-2 and the ensemble mean, but are overestimated in the 0°–30° N latitude band (Fig. 2d–e).

3.2 Vertical aerosol distributions

The vertical distributions of major aerosol species are shown in Fig. 3. Dust is concentrated primarily in the lower troposphere of the Northern Hemisphere (NH), particularly between 0° and 50° N, with concentrations exceeding $10\,\mathrm{\mu g\,m^{-3}}$ near 500 hPa (Fig. 3c). Sea salt aerosols are mainly confined to the lower troposphere below 700 hPa, particularly in the Southern Hemisphere (SH) (Fig. 3f). Anthropogenic aerosols, including sulfate and BC, are mainly concentrated below 500 hPa and within the latitudinal band of 20°–40° N, while OC shows enhanced concentrations near the equator and around 30° N (Fig. 3i, l, and o). Compared with MERRA-2 and the CMIP6 MME, CMA-CPSv4 reproduces the main lower-tropospheric distribution patterns of aerosol concentrations. However, over the tropical and subtropical region (0°–30° N), CMA-CPSv4 simulates aerosol layers extending to higher altitudes, particularly for dust, sea salt, and BC. Such differences are closely related to the stronger upward motion simulated over the tropical re-

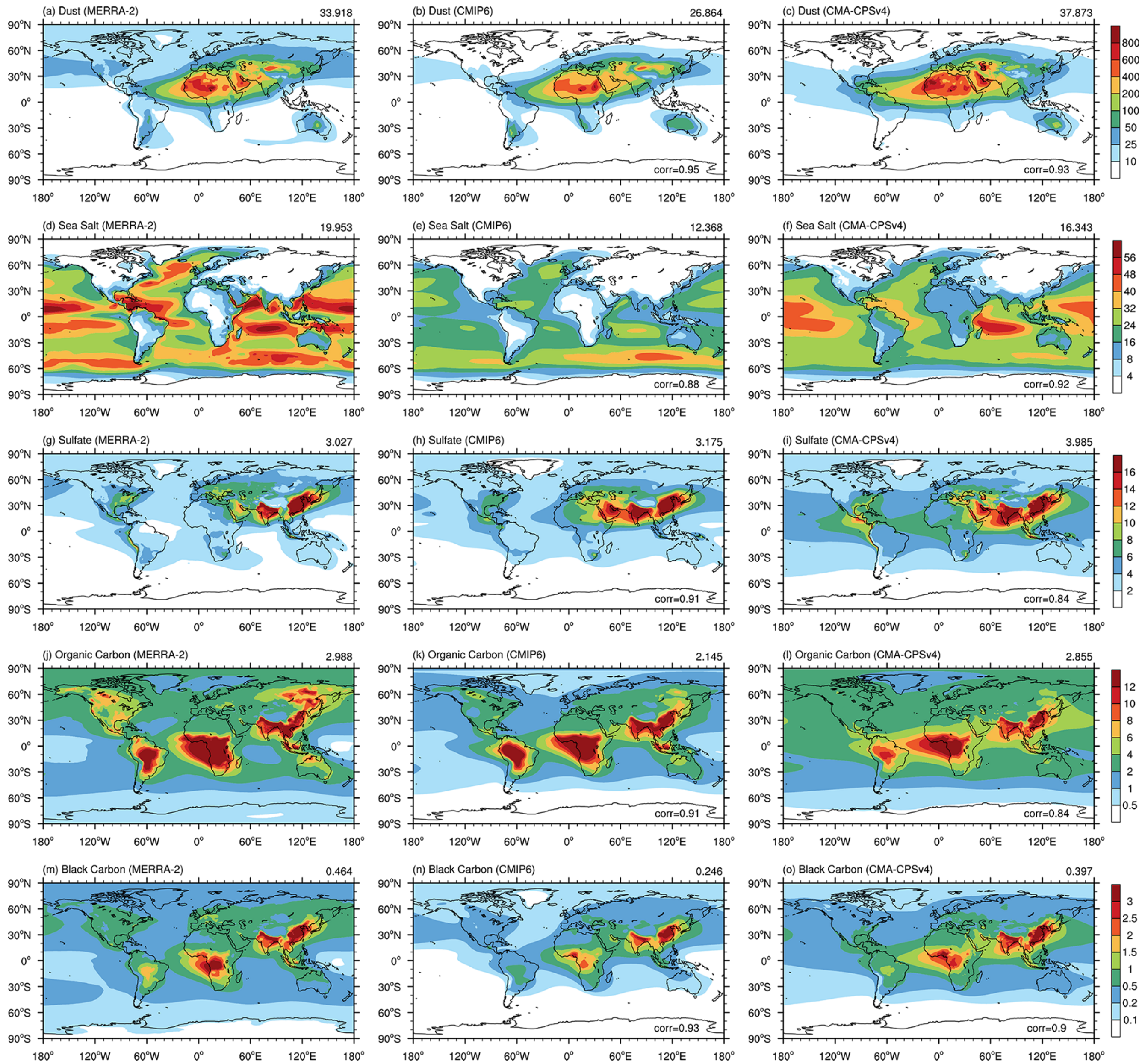

Figure 1. Spatial distribution of annual mean aerosol column mass concentrations (units: $mg\,m^{-2}$) of dust, sea salt, sulfate, organic carbon (OC), black carbon (BC) from Modern-ERA Retrospective Analysis for Research and Application (MERRA-2, left column), CMIP6 multi-model ensemble mean (CMIP6-MME, middle column) and CMA-CPSv4 simulations (right column) over the 2001–2020 period. The number at the top right of the panel is the global average of aerosol column mass concentrations. The number at the bottom right of the panel is the spatial correlation coefficient between CMIP6 MME, CMA-CPSv4 and MERRA-2, respectively.

gion (figure omitted), which enhances the vertical transport of boundary-layer aerosols into the upper troposphere. As a result, aerosols, including BC, are transported to higher altitudes over the 0°–30° N region in CMA-CPSv4 than in MERRA-2. In addition, the deep convection parameterization used in CMA-CPSv4 (Wu, 2012; Wu et al., 2019) may also contribute to transporting aerosols to higher altitudes through deep convective uplift and associated convective detrainment in the upper troposphere. Furthermore, because nudging constrains large-scale prognostic variables toward ERA5 reanalysis fields, it may suppress small-scale circulation variability and related precipitation processes, thereby weakening aerosol wet scavenging and allowing aerosols to persist at higher levels. These processes jointly contribute to the upward extension of aerosol layers in CMA-CPSv4 over the 0°–30° N region relative to MERRA-2.

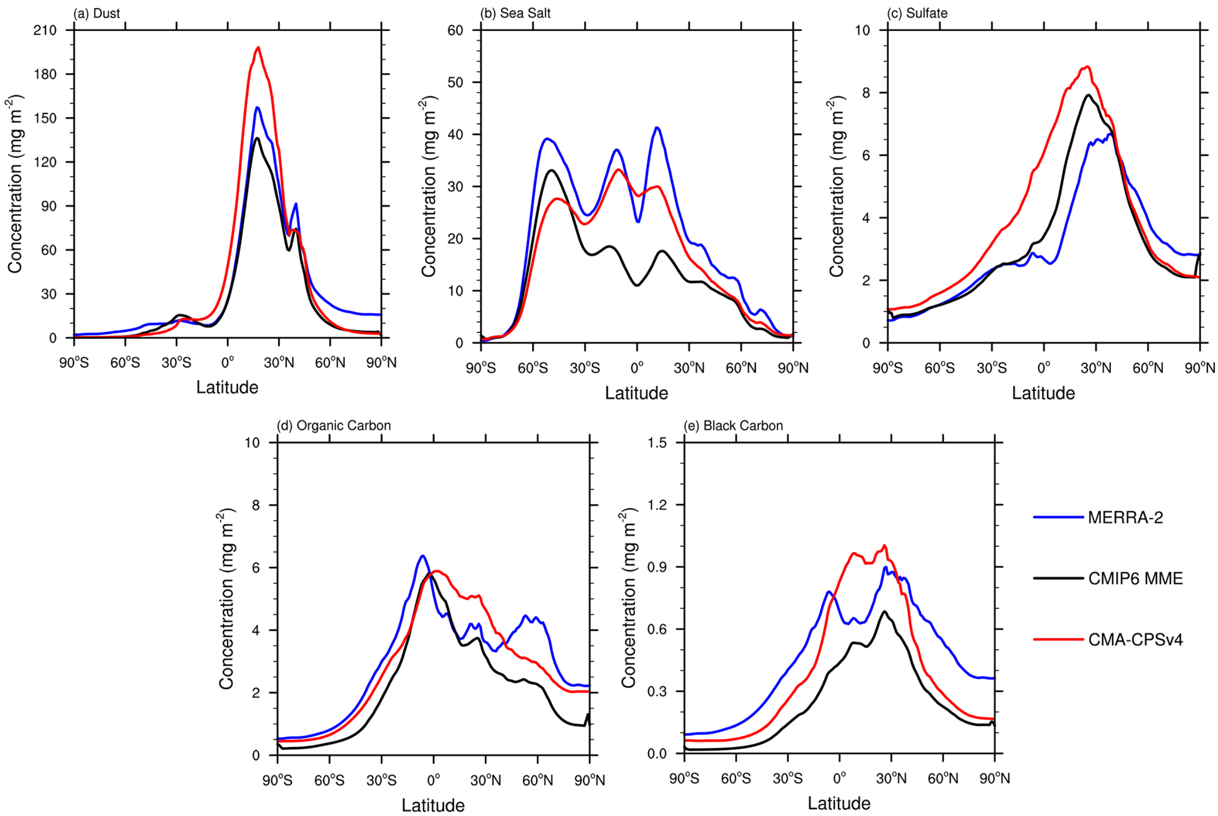

Figure 2. Annual zonal average of mean aerosol column mass concentrations (units: $mg\,m^{-2}$) of **(a)** dust, **(b)** sea salt, **(c)** sulfate, **(d)** OC, and **(e)** BC from MERRA-2, CMIP6 MME and CMA-CPSv4 simulations over the 2001–2020 period.

3.3 Seasonal variations of $PM_{2.5}$

Figure 4 presents monthly variations in regional surface $PM_{2.5}$ concentrations simulated by CMA-CPSv4, compared with the CMIP6 MME and MERRA-2 reanalysis. Over oceanic regions, MERRA-2 exhibits substantially higher surface $PM_{2.5}$ concentrations than both CMA-CPSv4 and the multi-model ensemble, primarily due to an overestimation of surface sea salt aerosols in MERRA-2 (Buchard et al., 2017; Provençal et al., 2017; Randles et al., 2017). In contrast, CMA-CPSv4 simulates $PM_{2.5}$ concentrations more consistent with the multi-model ensemble mean across the oceans (Fig. 4a). For East Asia, CMA-CPSv4 reproduces the spring $PM_{2.5}$ concentration peaks but underestimates the magnitude relative to both MERRA-2 and the ensemble mean (Fig. 4b). In the EMEP-East region, the model reasonably captures the seasonal variability but slightly overestimates concentrations during spring and autumn compared to the multi-model ensemble mean (Fig. 4c). Over North America, CMA-CPSv4 reproduces the annual cycle of surface $PM_{2.5}$ in the CMIP6 MME, including the summer (JJA) maximum, (Fig. 4f). CMA-CPSv4 also reproduces the monthly variability of $PM_{2.5}$ well in other regions – South Asia, Southeast Asia, the southern and eastern Mediterranean, and most land areas of the Southern Hemisphere – with correlation coefficients of 0.74, 0.88, 0.83, and 0.93, respectively (Fig. 4f, h, i and j). However, large biases remain over the EMEP-West region, Mexico, Central America, and the Caribbean (Fig. 4d and e). Overall, the annual $PM_{2.5}$ cycle in the CMIP6 MME is broadly consistent with MERRA-2 across most global regions. Nonetheless, both CMA-CPSv4 and the ensemble mean tend to underestimate $PM_{2.5}$ concentrations in the Northern Hemisphere (excluding East Asia) and over the oceans relative to MERRA-2. The annual cycle simulated by CMA-CPSv4 aligns more closely with the CMIP6 MME than with MERRA-2.

3.4 Interannual variations in Aerosols

The comparisons of interannual variations in surface dust, anthropogenic aerosols, and $PM_{2.5}$ concentrations across four major aerosol source regions: East Asia, South Asia, the southern Mediterranean, and South Africa are shown in Fig. 5. For dust aerosols, the CMA-CPSv4 captures interannual variations across three regions: South Asia, the southern Mediterranean, and South Africa. The simulated temporal evolution and trends are consistent with MERRA-2, but systematic underestimations exist, particularly in East Asia and South Asia (Fig. 5a and b). The temporal variations of anthropogenic aerosols and $PM_{2.5}$ exhibit similar features.

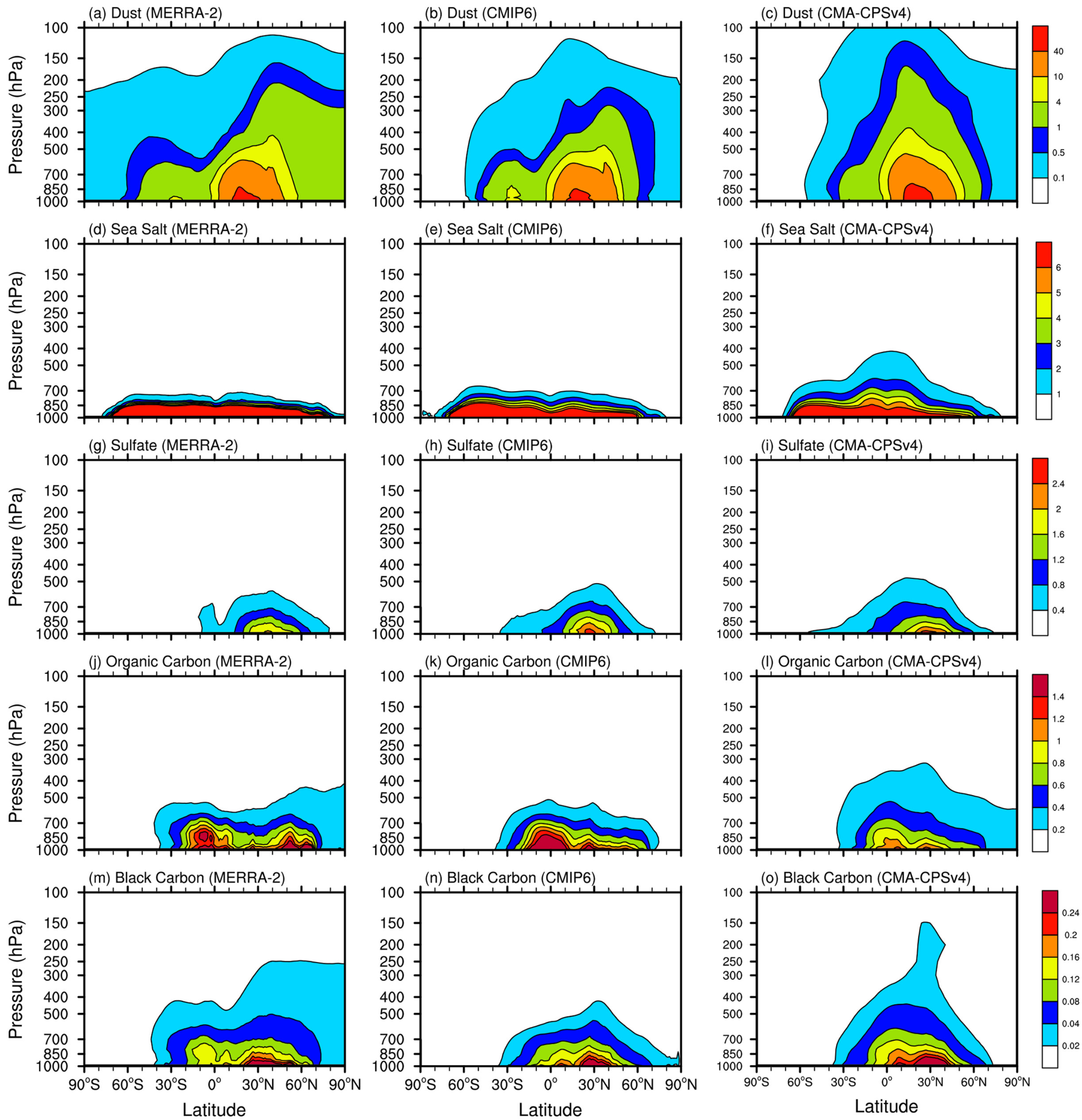

Figure 3. Latitude–pressure distributions of zonally averaged annual mean dust, sea salt, sulfate, OC and BC aerosol concentrations (units: $\mu g\, m^{-3}$) from MERRA-2 (left column), CMIP6 MME (middle column) and CMA-CPSv4 (right column) over the 2001–2020 period.

In East Asia, both anthropogenic aerosols and $PM_{2.5}$ show an increasing trend between 2001 and 2012, followed by a decline (Fig. 5e and i). In South Asia, both aerosols show statistically significant upward trends, with growth rates exceeding those in other regions (Fig. 5f and j). In contrast, trends in the southern Mediterranean and southern Africa are weaker (Fig. 5g, h, k and l). Simulations of both anthropogenic aerosols and $PM_{2.5}$ are correlated with MERRA-2, with correlation coefficients exceeding 0.71 in East Asia, South Asia, and South Africa. Overall, CMA-CPSv4 reasonably reproduces the interannual variations and trends of surface dust, anthropogenic aerosols, and $PM_{2.5}$ across these major aerosol source regions, though simulated concentrations still exhibit deviations.

3.5 East Asia $PM_{2.5}$ concentrations

Figure 6 presents the spatial distribution of annual mean surface $PM_{2.5}$ concentrations at 392 monitoring sites across East Asia, derived from CNEMC and EANET observations, MERRA-2 reanalysis, the CMIP6 MME, and CMA-

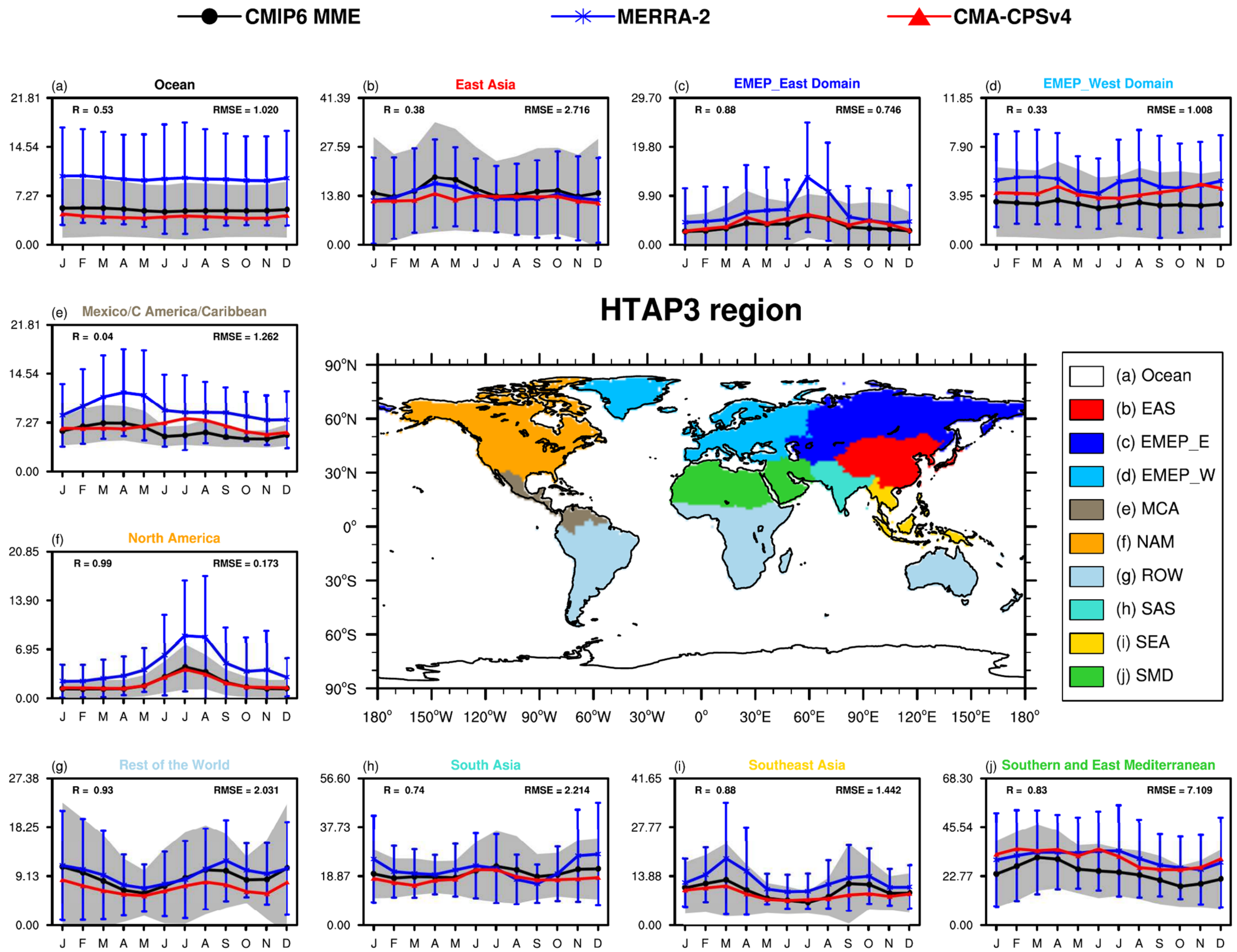

Figure 4. Monthly variations of surface $PM_{2.5}$ concentrations (units: $\mu g\,m^{-3}$) from MERRA-2 (blue line), CMIP6 MME (black line) and CMA-CPSv4 (red line) for different regions of the world during 2001–2020. The gray shading and blue error bars show the regional variability in the values of the multi-model ensemble mean and MERRA-2, respectively. The upper-left and upper-right corners of each panel show the correlation coefficient (R) and root mean square error (RMSE) between CMA-CPSv4 and CMIP6 MME. The middle panel shows the nine regions (EAS, EMEP_E, EMEP_W, MCA, NAM, ROW, SAS, SEA, SMD) of the globe as defined by the Task Force on Hemispheric Transport of Air Pollutants (TF HTAP3), as well as the ocean.

CPSv4 simulations averaged over 2001–2020. Compared with observations from CNEMC and EANET, MERRA-2, the CMIP6 MME, and CMA-CPSv4 all underestimate annual mean $PM_{2.5}$ concentrations across East Asia (Fig. 6b, c and d). The CMA-CPSv4 results are broadly consistent with the CMIP6 MME but underestimate the observed $PM_{2.5}$ values by up to $20\,\mu g\,m^{-3}$ in high-concentration regions of eastern China (Fig. 6c and d). In addition, the model also distinctly underestimates $PM_{2.5}$ concentrations in the Taklamakan–Mongolia–North China region, primarily due to its underestimation of dust concentrations in this area (Fig. 6a and d).

Figure 7 further compares simulated and observed $PM_{2.5}$ concentrations through scatter plots of CMA-CPSv4 against ground-based observations, MERRA-2, and the CMIP6 MME. Relative to the CMIP6 MME and MERRA-2, CMA-CPSv4 reproduces the spatial variability of $PM_{2.5}$ well, with correlation coefficients of 0.95 and 0.90, respectively (Fig. 7b, c). The simulated values are generally distributed close to the 1 : 1 line, although CMA-CPSv4 tends to be slightly lower than MERRA-2. In contrast, CMA-CPSv4 substantially underestimates $PM_{2.5}$ concentrations compared to site observations, with simulated values averaging only about half of the observed levels, indicating a low bias in model performance over East Asia. Such underestimation of $PM_{2.5}$ concentrations is a common issue among CMIP6 models (Ren et al., 2024; Turnock et al., 2020; Zhang et al., 2012). The differences between CMIP6 models and obser-

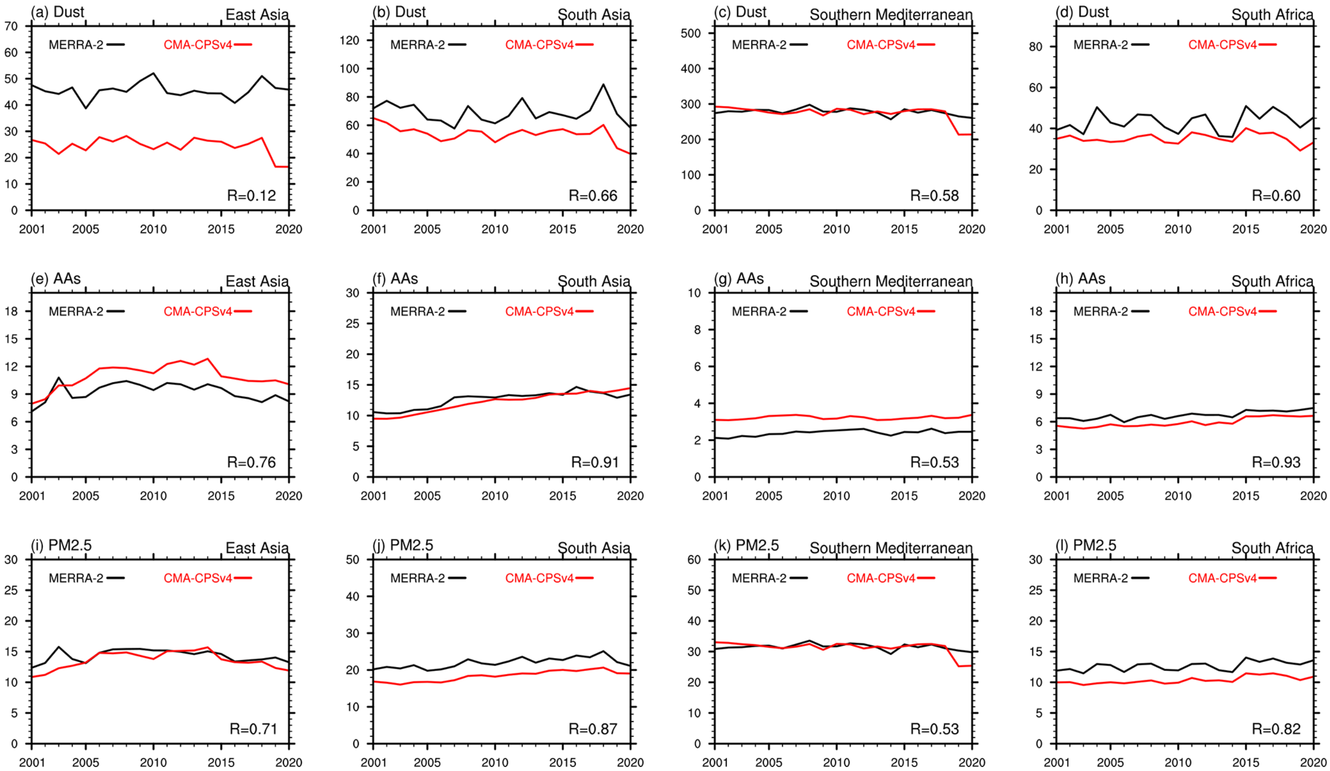

Figure 5. Temporal evolution of surface concentrations (units: $\mu g\,m^{-3}$) of dust **(a–d)**, anthropogenic aerosols including sulfate, OC and BC **(e–h)** and $PM_{2.5}$ **(i–l)** from MERRA-2 (black line) and CMA-CPSv4 simulations (red line) over East Asia (left column), South Asia (second column), the southern Mediterranean (third column), and south Africa (right column) over the 2001–2020 period. The number at the bottom right of the panel is the spatial correlation coefficient between CMA-CPSv4 simulations and MERRA-2.

vations may partly result from uncertainties in the partitioning of natural aerosols into the $PM_{2.5}$ fraction, as well as the omission of secondary organic aerosols, ammonium, and nitrate in $PM_{2.5}$ calculations (Shrivastava et al., 2017; Zheng et al., 2015).

3.6 Aerosol optical depth

This section further assesses the model performance in reproducing the global distribution and seasonal variations of AOD. The spatial pattern of AOD is modulated by aerosol composition, concentration, and the influence of clouds. Figure 8 presents the spatial distribution of the global annual mean AOD derived from AERONET, MERRA-2, MISR, MODIS, CMIP6 MME and CMA-CPSv4 simulations, averaged over the period 2001–2020. On a global scale, high AOD areas are mainly located in North Africa, the Middle East, South Asia, and East Asia within the Northern Hemisphere (Fig. 8a–f). In these source regions, the simulated AOD magnitudes in the high-value areas are comparable to those from AERONET, MODIS and CMIP6 MME (Fig. 8a, c, e and f), while slightly exceeding the values from MERRA-2 and MISR (Fig. 8b and d). The simulated spatial pattern of AOD over North America is broadly consistent with AERONET observations and CMIP6 MME. Over oceanic regions, the CMA-CPSv4 simulation shows similar spatial distributions to MERRA-2 data and CMIP6 MME. High AOD values observed by MISR, MERRA-2, and CMIP6 MME near 60° S, primarily associated with high sea salt concentrations, are also reproduced by CMA-CPSv4 (Fig. 8b, d, e and f). Despite these agreements, certain regional biases remain. For instance, the model overestimates AOD over Europe, western North Africa, and southern China relative to the observations. Overall, the simulated AOD from CMA-CPSv4 captures the principal spatial distribution features consistent with AERONET, satellite datasets, MERRA-2 and CMIP6 MME on the global scale, with a correlation coefficient of 0.81 with AERONET observations. The global mean AOD simulated by CMA-CPSv4 (0.1271) is slightly higher than that from MERRA-2 (0.1191), CMIP6 MME (0.117) and MISR (0.1186), which is within the uncertainty range (±0.05) of the MISR AOD detection (Kahn et al., 1998).

The comparisons of monthly mean AOD simulated by CMA-CPSv4 with observations from AERONET, MERRA-2 reanalysis, and CMIP6 MME are presented in Fig. 9. A total of 5275 data pairs is analyzed, including 2988 data pairs for the comparison with the CMIP6 MME. The simulated

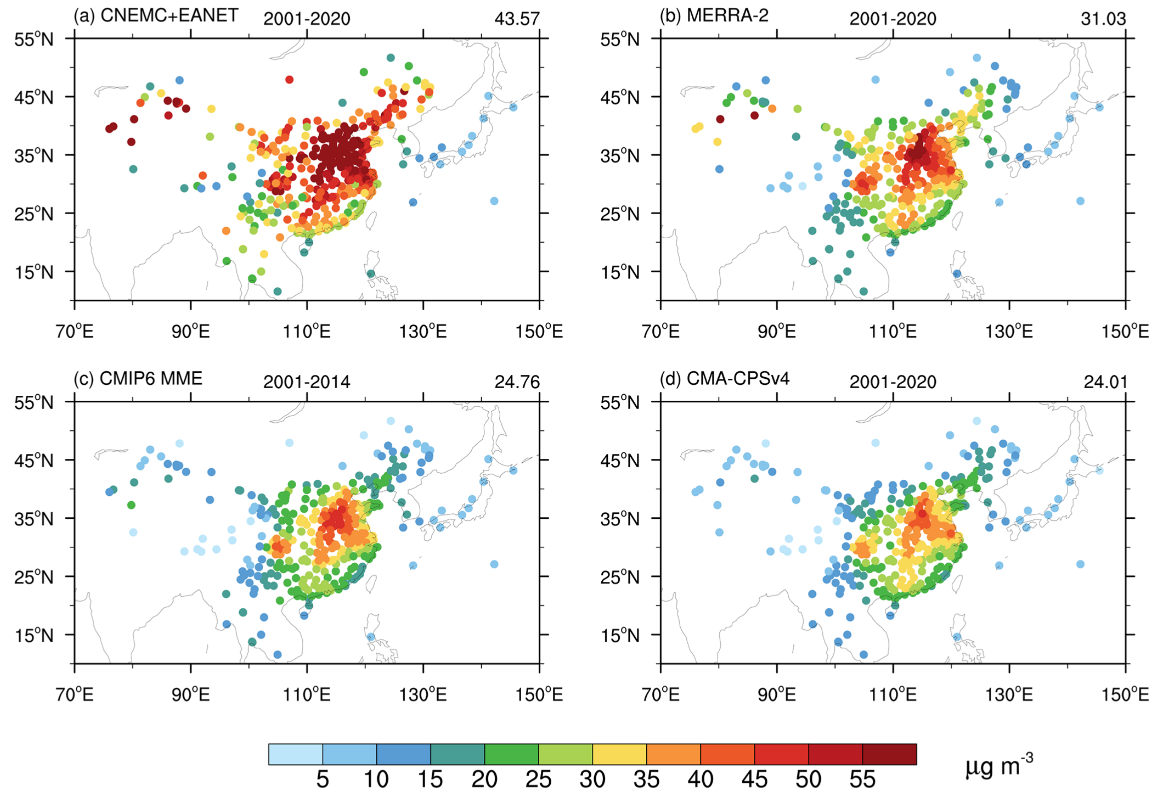

Figure 6. Spatial distribution of annual mean surface $PM_{2.5}$ concentrations (units: $\mu g\,m^{-3}$) at 392 monitoring sites from **(a)** EANET (28 sites) and CNEMC (364 sites) in Asia. Corresponding simulation in **(b)** MERRA-2, **(c)** CMIP6 MME, and **(d)** CMA-CPSv4 over the 2001–2020 period. The number at the top right of the panel is the mean surface $PM_{2.5}$ concentrations at the 392 monitoring sites.

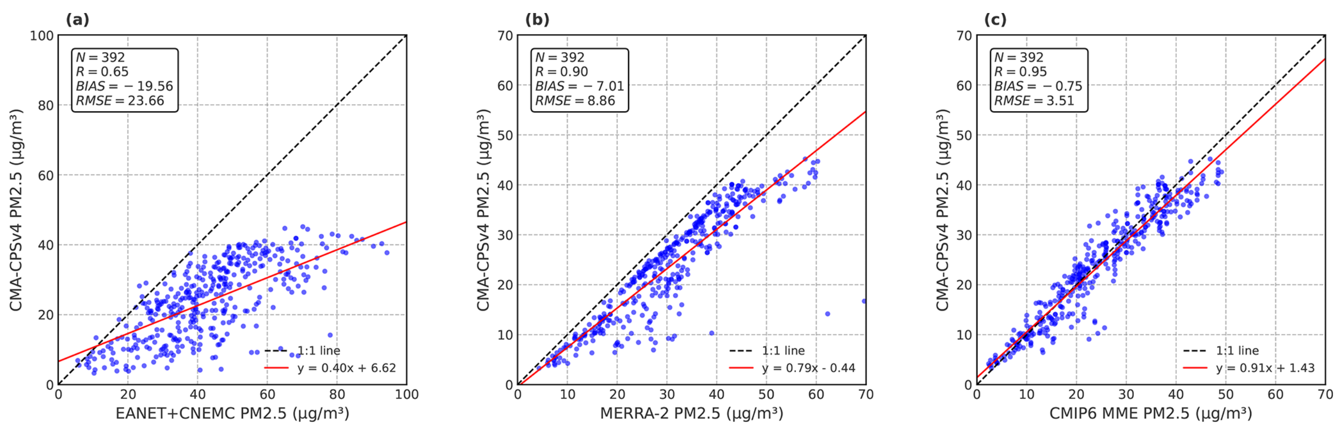

Figure 7. Scatter plots of annual mean surface $PM_{2.5}$ concentrations (units: $\mu g\,m^{-3}$) of CMA-CPSv4 simulations against **(a)** the observations from EANET and CNEMC sites, **(b)** MERRA-2, and **(c)** CMIP6 MME, respectively. The solid black line and red line in the scatterplot represent the 1 : 1 reference line and the linear regression line, respectively. The top left corner of each panel shows the performance metrics.

AOD intensity closely matches the AERONET AOD intensity at the vast majority of locations, although slight underestimation occurs at a few sites (Fig. 9a). The underestimation likely results from spatial averaging of high-emission sources within coarse-resolution grid cells, which smooths localized emission peaks in the simulation results. Compared with MERRA-2 and the CMIP6 MME, CMA-CPSv4 exhibits higher correlations and lower RMSEs (Fig. 9b, c). The correlation coefficient between simulated and AERONET AOD is 0.78, increasing to 0.84 and 0.88 for MERRA-2 and the CMIP6 MME, respectively. The corresponding root mean square errors (RMSEs) decrease to 0.071 and 0.065 for MERRA-2 and CMIP6 MME, respectively, compared with 0.095 for AERONET. These results indicate that the

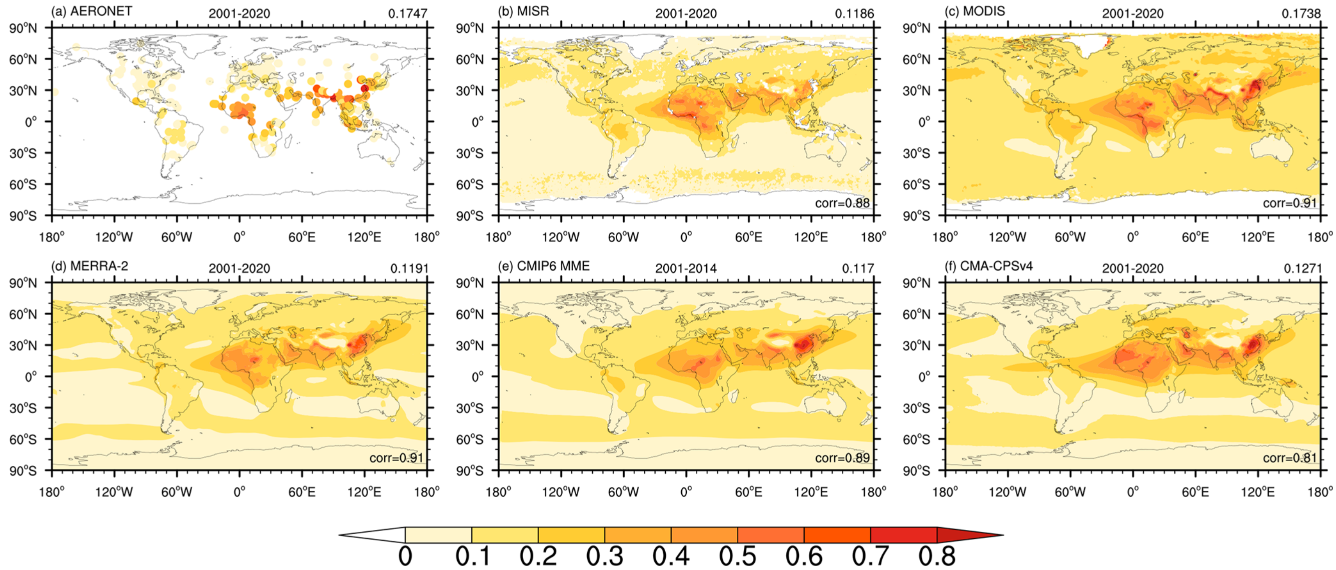

Figure 8. Spatial distribution of annual mean AOD at 550 nm over the 2001–2020 period from **(a)** Aerosol Robotic Network (AERONET), **(b)** the Multiangle Imaging Spectroradiometer (MISR) instrument, **(c)** Moderate Resolution Imaging Spectroradiometer (MODIS) Aqua and Terra, **(d)** MERRA-2, **(e)** CMIP6 MME (2001–2014 only), and **(f)** CMA-CPSv4 simulations. The number at the top right of the panel is the global average of AOD. The number at the bottom right of each panel is the global spatial correlation coefficient between AOD at 550 nm from AERONET site locations and the corresponding values from MISR, MODIS, MERRA-2, CMIP6 MME, and CMA-CPSv4 simulations.

simulated AOD is more consistent with MERRA-2 and the CMIP6 MME than with AERONET observations. Overall, the simulated AOD can capture the observed variability, with correlation coefficients exceeding 0.78 for all three reference datasets.

Figure 10 presents the monthly variations of simulated AOD from CMA-CPSv4 compared with AERONET observations, MERRA-2 reanalysis and CMIP6 MME across different regions. In general, the simulated AOD is within the error range of the observations. The model reproduces the annual cycle of AOD reasonably well in several regions, particularly over North America, the southern and eastern Mediterranean, the ocean, and Southern Hemisphere land areas, with correlation coefficients (R) of 0.95, 0.94, 0.86, and 0.83, respectively (Fig. 10a, f, g and j). The CMIP6 MME is also relatively close to AERONET and MERRA-2 in these regions. However, CMA-CPSv4 notably overestimates AOD during June–August (JJA) in most regions, including Mexico, Central America, the Caribbean, South Asia, Southeast Asia, and the EMEP-West region (Fig. 10d, e, h and i). Moreover, the simulated AOD peaks in these regions occur later in the CMA-CPSv4 (summer) compared to observations (spring), likely due to an overestimation of summertime sulfate aerosol concentrations by CMA-CPSv4. In East Asia, CMA-CPSv4 captures the general seasonal variation patterns during spring and summer but underestimates their intensity, while AOD values are overestimated during autumn (Fig. 10b). In Southeast Asia and the EMEP-East region, the model fails to reproduce the observed amplitude of seasonal variation, showing weaker seasonality compared with AERONET and MERRA-2 (Fig. 10d and i). Large differences between the CMIP6 MME and both AERONET and MERRA-2 are also evident over East Asia, the EMEP-East region, South Asia, and Southeast Asia (Fig. 10b, c, h and i), suggesting that accurately simulating aerosol seasonal variations in these regions remains challenging for current ESMs.

3.7 Case analysis of pollution events in China

In the previous sections, the performance of CMA-CPSv4 in reproducing aerosol concentrations and AOD distributions was systematically evaluated against observations, the MERRA-2 reanalysis and the CMIP6 MME. To further assess model performance during high-pollution conditions, this section presents an evaluation of $PM_{2.5}$ pollution events in terms of their spatial occurrence frequency distributions and temporal evolution at representative sites. In addition, we selected two severe dust pollution events to evaluate the model's ability to reproduce such pollution events.

Figure 11 shows the spatial distributions of $PM_{2.5}$ pollution-event occurrence frequencies over China during 2014–2019 from CNEMC observations, MERRA-2 reanalysis, and CMA-CPSv4 simulations. For mild pollution events ($35\,\mu g\,m^{-3} \leq PM_{2.5}$ mass $< 75\,\mu g\,m^{-3}$), such events occur frequently across most regions of China, with occurrence frequencies generally exceeding 10 % and reaching more than 30 % over the North China Plain, the Yangtze River Delta, and the Sichuan Basin (Fig. 11a). Both MERRA-2 and CMA-CPSv4 reproduce the major spatial distribution fea-

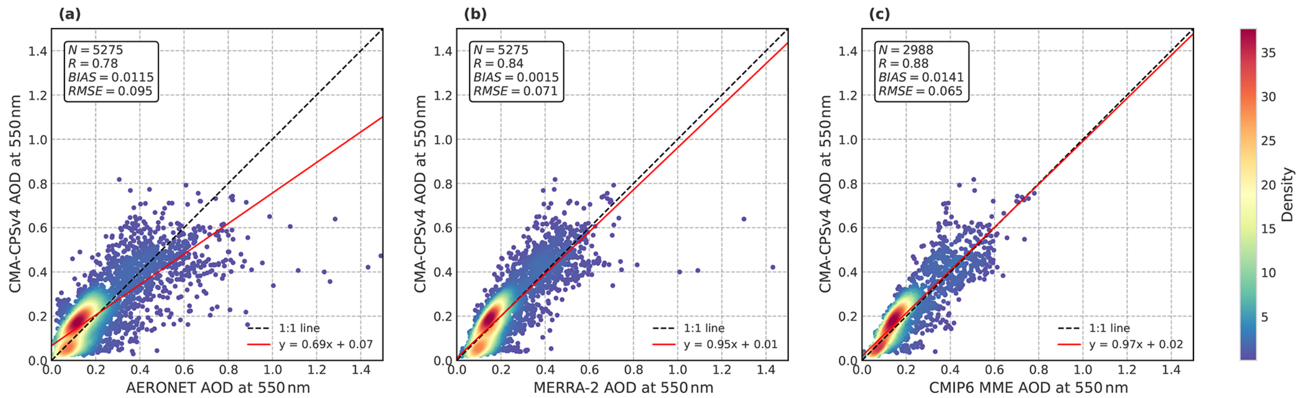

Figure 9. Scatter plots of monthly mean CMA-CPSv4 AOD at 550 nm against **(a)** AERONET AOD at 550 nm, **(b)** MERRA-2 AOD at 550 nm, and **(c)** CMIP6 MME AOD at 550 nm, respectively. The solid black line and red line in the scatterplot represent the 1 : 1 reference line and the linear regression line, respectively. The color represents the density of data points. The top left corner of each panel shows the performance metrics.

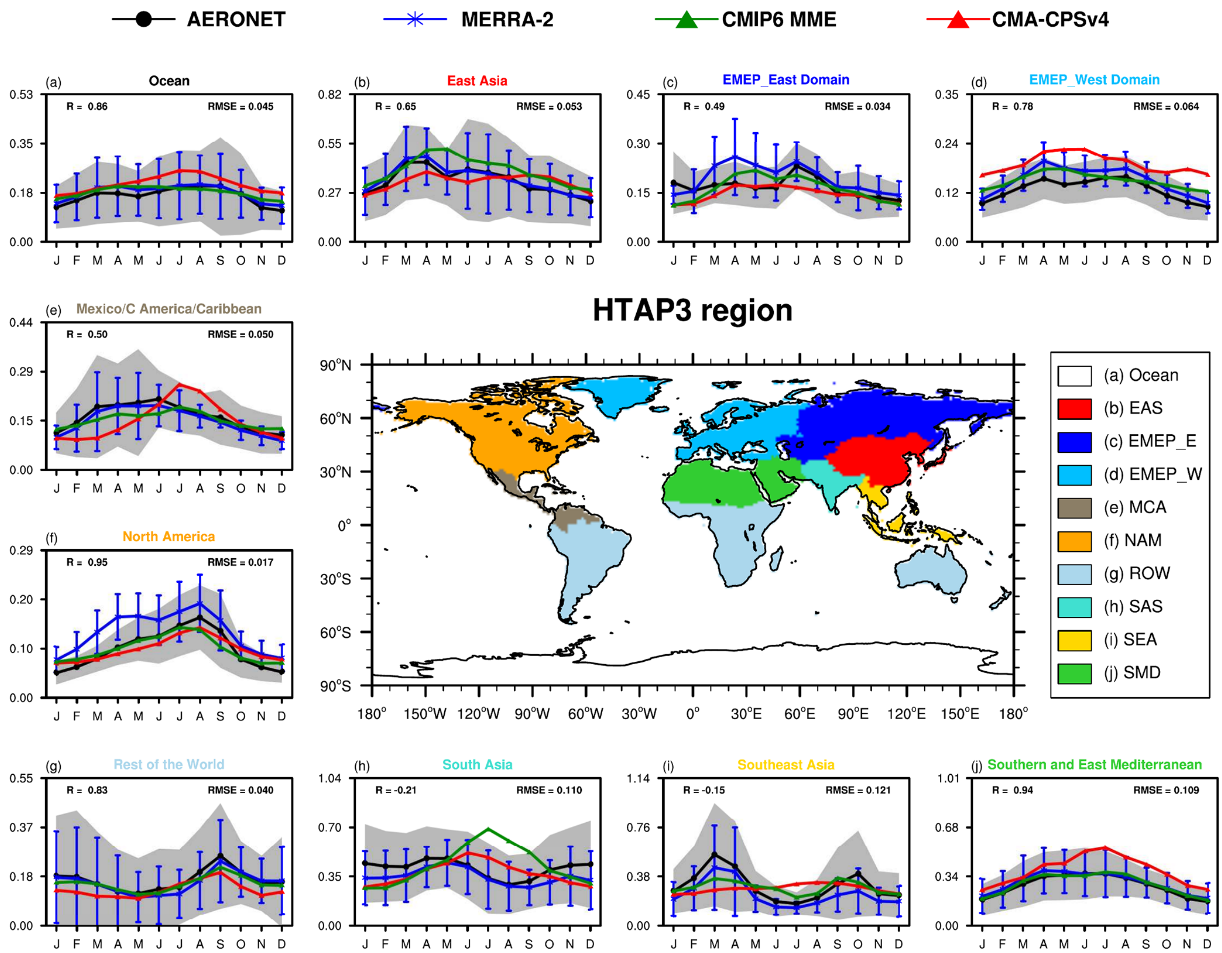

Figure 10. Monthly variations of AOD at 550 nm from AERONET (black line), MERRA-2 (blue line), CMIP6 MME (green line) and CMA-CPSv4 (red line) for different regions of the world during 2001–2020. The gray shading and blue error bars show the regional variability in the values of AERONET and MERRA-2, respectively. The upper-left and upper-right corners of each panel show the correlation coefficient (R) and root mean square error (RMSE) between CMA-CPSv4 and AERONET. The middle panel shows the nine regions (EAS, EMEP_E, EMEP_W, MCA, NAM, ROW, SAS, SEA, SMD) of the globe as defined by the Task Force on Hemispheric Transport of Air Pollutants (TF HTAP3), as well as the ocean.

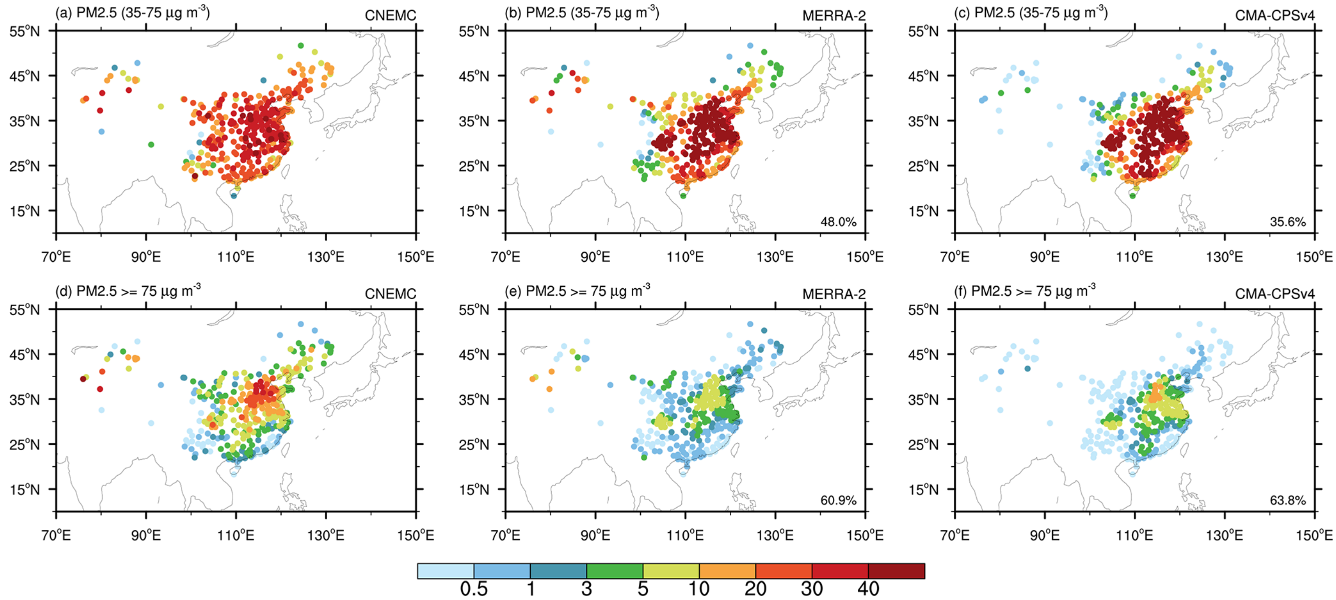

Figure 11. Spatial distributions of $PM_{2.5}$ pollution-event occurrence frequencies (%) over China for the period 2014–2019 from CNEMC observations, MERRA-2, and CMA-CPSv4 simulations, respectively. Panels **(a–c)** show mild pollution events ($35\,\mu g\,m^{-3} \leq PM_{2.5}$ mass $< 75\,\mu g\,m^{-3}$), while panels **(d–f)** show moderate-to-severe pollution events ($PM_{2.5}$ mass $\geq 75\,\mu g\,m^{-3}$). Values in the lower-right corners of panels **(b)**, **(c)**, **(e)**, and **(f)** represent the proportion of stations at which the absolute deviation between simulated and observed occurrence frequencies is below 10 %.

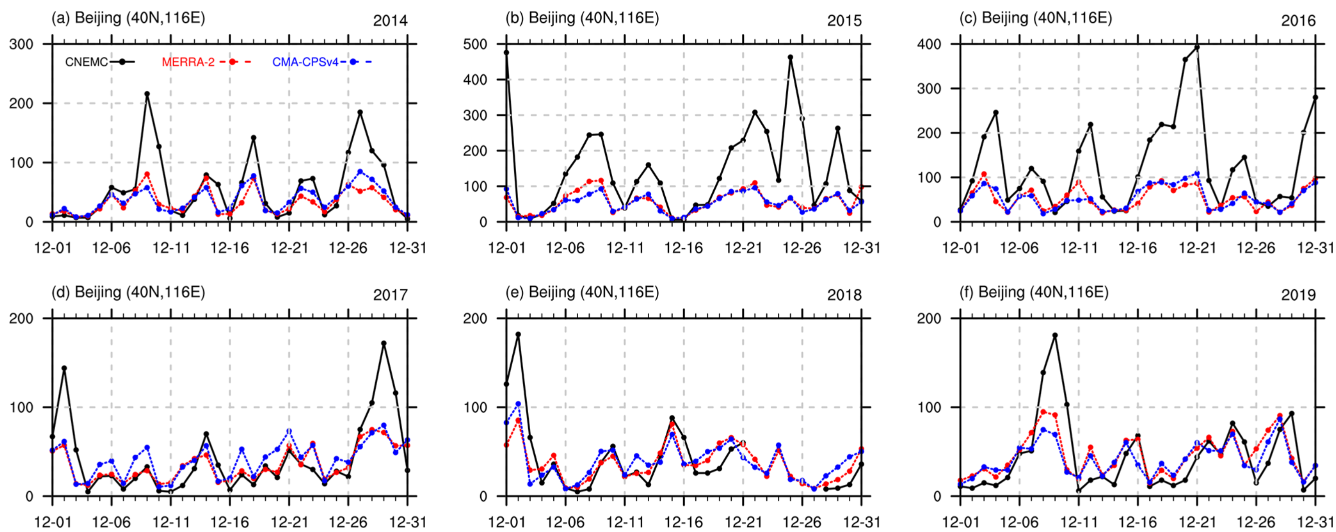

Figure 12. Daily evolution of $PM_{2.5}$ concentrations during December for 2014–2019 at Beijing site (40° N, 116° E), derived from CNEMC observations (black line), MERRA-2 (red line), and CMA-CPSv4 simulations (blue line).

tures, particularly over the Yangtze River Delta, the Sichuan Basin, and central China, although occurrence frequencies are slightly higher in these regions (Fig. 11b, c). Similar spatial patterns are found in MERRA-2 and CMA-CPSv4 for mild pollution events. Negative deviations relative to observations are mainly concentrated over the Taklamakan Desert, Gansu, Inner Mongolia, and parts of southwestern China (Fig. 11c), likely associated with the underestimation of dust concentrations in CMA-CPSv4. Approximately 35.6 % and 48.0 % of stations in CMA-CPSv4 and MERRA-2, respectively, exhibit absolute deviations within the 10 % error threshold. For moderate-to-severe pollution events ($PM_{2.5}$ mass $\geq 75\,\mu g\,m^{-3}$), underestimations are mainly found over the North China Plain, northeastern China, and southwestern China (Fig. 11e and f). Relative to MERRA-2, CMA-CPSv4 shows smaller deviations at some stations over the North

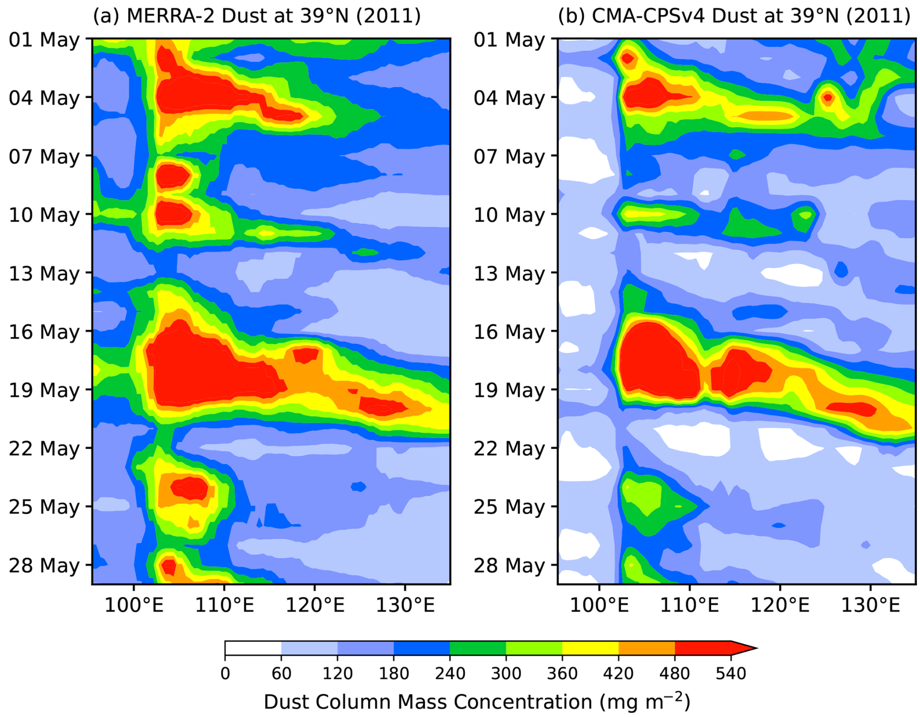

Figure 13. Longitude-time Hovmöller diagrams of dust column mass concentrations (units: $mg\,m^{-2}$) of **(a)** MERRA-2 (left column) and **(b)** CMA-CPSv4 (right column) from 1 to 30 May 2011 averaged from 37.5° N to 38.5° N in eastern China (95° E–135° E).

China Plain, although underestimations persist over the Taklamakan Desert, Gansu, and Inner Mongolia (Fig. 11f). Meanwhile, 60.9 % and 63.8 % of stations in MERRA-2 and CMA-CPSv4 satisfy the 10 % absolute-deviation criterion relative to observations. These results indicate that both datasets tend to underestimate the occurrence frequency of pollution events.

To further evaluate the model's performance in reproducing the temporal evolution of pollution episodes, the Beijing monitoring station on the North China Plain is selected as a representative site. This region experiences frequent pollution episodes in winter, primarily associated with enhanced anthropogenic aerosol emissions during this season. Figure 12 shows the daily evolution of $PM_{2.5}$ concentrations at the Beijing site between December 2014 and December 2019 from CNEMC observations, MERRA-2 reanalysis, and CMA-CPSv4 simulation. The temporal variations simulated by CMA-CPSv4 are broadly consistent with those from MERRA-2, including the timing, peak intensity, and duration of pollution episodes. Although both datasets significantly underestimated $PM_{2.5}$ concentrations during pollution episodes compared to observations, the timing and persistence of most pollution peaks are generally captured (Fig. 12a–f). Among the 31 pollution episodes identified during the study period, the timing of peak concentrations is reproduced in 27 cases, while the remaining four cases show peak occurrences advanced by one day. These results indicate that CMA-CPSv4 captures the temporal evolution and peak timing of pollution episodes in the North China Plain. The lower simulated $PM_{2.5}$ concentrations during pollution episodes are consistent with the general underestimation discussed in Sect. 3.5.

Here, we further examine the model's ability to reproduce severe dust pollution events. Figure 13 presents Hovmöller diagrams of dust mass concentration along 39° N from 1 to 30 May 2011. According to MERRA-2, two major dust transport events occurred during 1–6 May and 14–21 May 2011, respectively, with a minor dust episode observed around 9–10 May (Fig. 13a). The first major event originated near 100° E and propagated eastward to approximately 130° E, while the weaker mid-month event extended to about 125° E. The second major dust event (14–21 May) exhibited the highest intensity and widest transport extent, with dust plumes reaching the western Pacific around 140° E. CMA-CPSv4 successfully reproduces the temporal evolution and spatial progression of these dust plumes – from initial emissions over western China to their subsequent eastward transport – although the simulated dust intensity is slightly underestimated (Fig. 13b).

Figure 14 shows the spatial distribution of dust mass concentrations simulated by CMA-CPSv4 for the dust event over China during 15–21 May 2011, in comparison with MERRA-2 reanalysis data. Overall, the spatial pattern of dust concentrations reproduced by CMA-CPSv4 is consistent with that of MERRA-2. Initially, a dust plume develops over northwestern Inner Mongolia (Fig. 14a, b). Under the

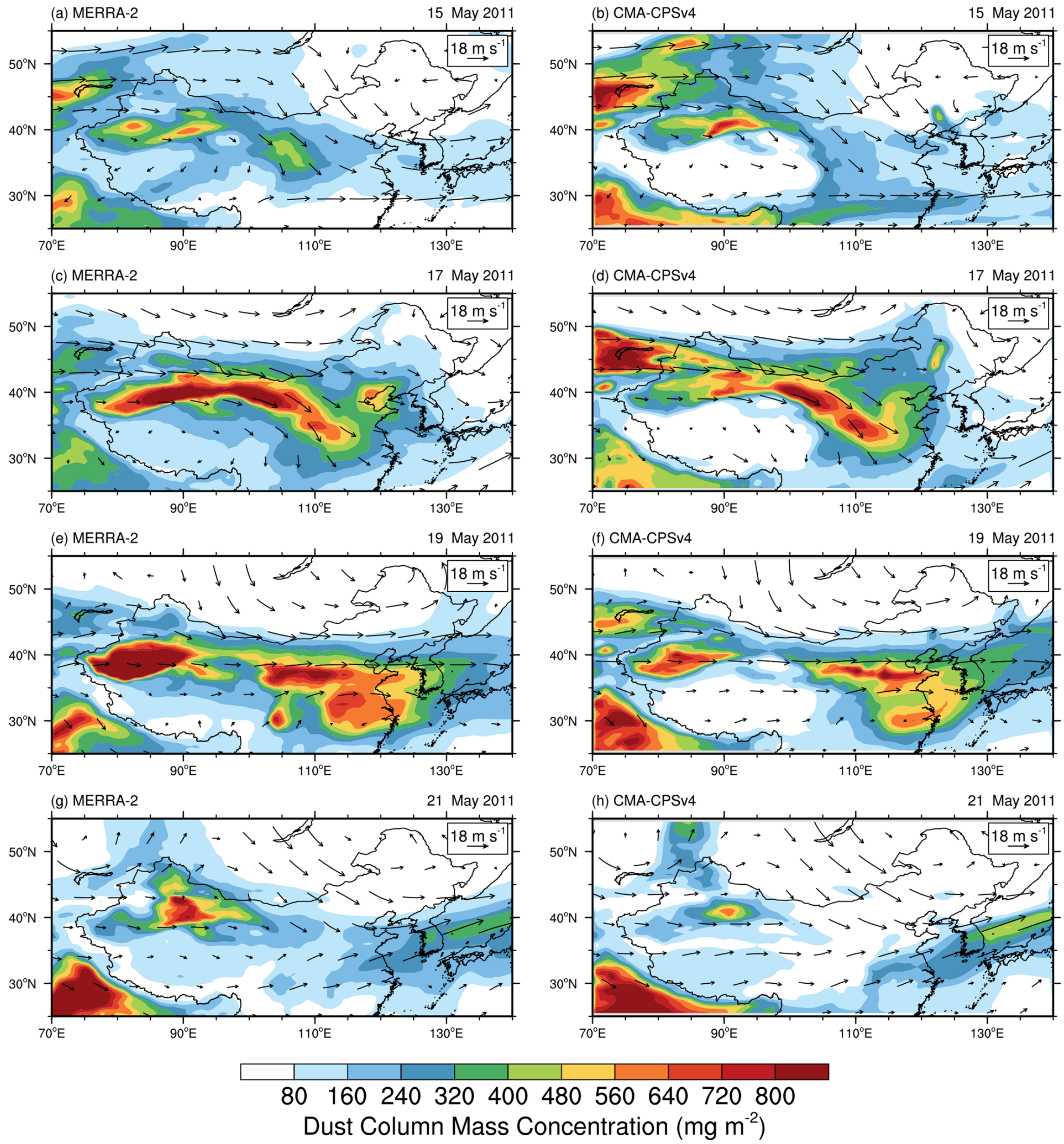

Figure 14. Spatial distribution of dust column mass concentrations (units: $\mathrm{mg\,m^{-2}}$) overlaid with 500 hPa wind vectors (units: $\mathrm{m\,s^{-1}}$) in China for the dust event from 15 to 21 May 2011, derived from MERRA-2 (left column) and CMA-CPSv4 (right column).

influence of large-scale circulation, the plume intensifies and propagates southeastward, affecting western and eastern Inner Mongolia, Northwest China, North China, Central China, and East China (Fig. 14c–f). Subsequently, the plume continues eastward and dissipates over the Pacific Ocean (Fig. 14g, h). The model successfully captures the temporal evolution and transport pathway of the dust plumes, indicating that CMA-CPSv4 can realistically reproduce the major features of dust emission and transport during this severe event.

Figure 15 compares the temporal evolution of dust concentrations at the Shandan Station during the 12–21 May 2011 dust event as simulated by CMA-CPSv4. The observed dust concentrations gradually increased from 12 May, peaked on 17 May, and were followed by a rapid decline reaching a minimum on 21 May. CMA-CPSv4 successfully reproduces the timing of the peak and the trends during this event, although it generally underestimates the magnitude relative to MERRA-2. Meteorological conditions on 16 May, the day preceding the peak, the largest differences in surface air and 500 hPa temperatures and maximum surface wind speed occurred in Shandan, resulting in unstable stratification and enhanced dust uplift and transport. CMA-CPSv4 captures the temperature gradient and wind speed variations reasonably well, though with a slight overestimation of surface winds.

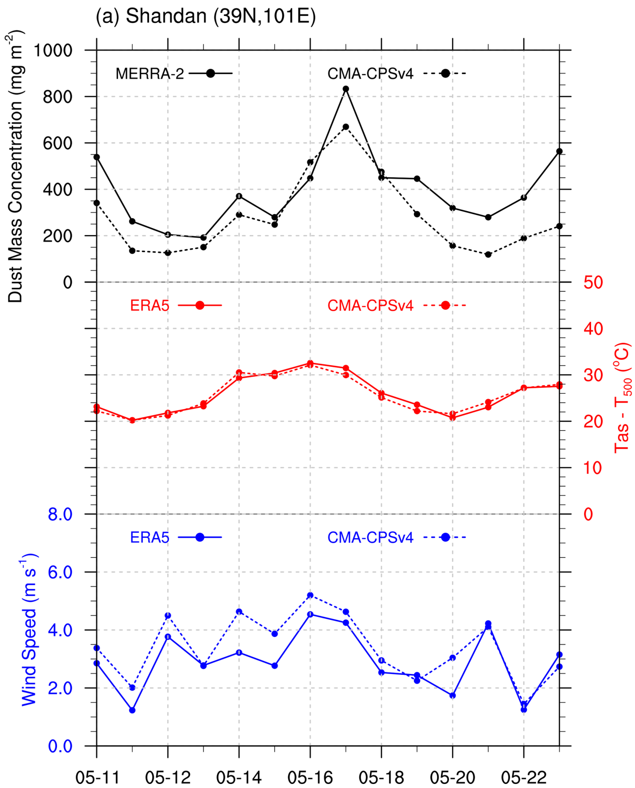

Figure 15. Time series of dust column mass concentration (units: $mg\,m^{-2}$), the difference between surface air temperature and 500 hPa layer air temperature (units: °C), and surface wind speed (units: $m\,s^{-1}$) of MERRA-2 (solid line) and CMA-CPSv4 (dashed line) during the dust event of 11–23 May 2011 in Gansu (38° N–40° N, 100° E–102° E).

Overall, the model demonstrates good performance in reproducing the temporal features and meteorological conditions of this dust pollution event.

4 Summary and discussion

In this study, the performance of the newly developed CMA-CPSv4 in simulating major aerosol species and aerosol optical depth (AOD) under the condition of the observed large-scale atmospheric circulation is systematically evaluated. The 20-year simulations from 2001 to 2020 for global distributions, seasonal and interannual variations of dust, sea salt, sulfate, organic carbon, black carbon, and AOD are compared with ground-based observations, the MERRA-2 reanalysis, and the CMIP6 MME. The main results show that:

1. CMA-CPSv4 reproduces the global distribution, seasonal variations and interannual variations of major aerosol species and aerosol optical depth (AOD) well, with spatial correlation coefficients exceeding 0.84 relative to observations, MERRA-2 and CMIP6 MME data. In particular, the simulated seasonal variations of $PM_{2.5}$ and AOD are consistent with CMIP6 MME and site observations over most regions, including North America, the southern and eastern Mediterranean, Southern Hemisphere land areas, and East Asia. In addition, simulations of $PM_{2.5}$ pollution episodes and extreme dust storm events in China show that CMA-CPSv4 captures the temporal evolution of $PM_{2.5}$ and dust pollution, as well as the associated meteorological conditions, with event frequency, peak intensity, and duration comparable to those in MERRA-2.
2. Over East Asia, simulated $PM_{2.5}$ concentrations are comparable to those from the CMIP6 MME. However, the model systematically underestimates observed $PM_{2.5}$ values. This underestimation may be partly due to uncertainties in the partitioning of natural aerosols into the $PM_{2.5}$ fraction and the use of an approximate method to calculate $PM_{2.5}$, which disregards contributions from other aerosols, such as secondary organic aerosols, nitrate and ammonium aerosols.
3. There also exist notable regional biases for aerosol simulations in CMA-CPSv4, especially in the simulation for dust and sulfate aerosols. The CMA-CPSv4 underestimates dust concentrations over the Taklamakan Desert–Mongolia region and northern China. The simulated sulfate aerosols over the oceans have also been overestimated, primarily due to the overestimation of model-simulated DMS emissions from oceanic phytoplankton activity. The evaluation of the vertical distribution indicates that CMA-CPSv4 simulates stronger upward transport of aerosols from the surface to the upper troposphere in tropical regions compared with MERRA-2 and the CMIP6 MME.

All comparisons demonstrate that the aerosol module implemented in CMA-CPSv4 provides reliable aerosol simulations for the BCC-CSM2-HR, which are the foundation for aerosol prediction in the CMA-CPSv4. The next work will focus on investigating aerosol-climate interactions and the impact of aerosols on numerical weather and climate prediction.

Code availability. All simulations used in this work were performed using CMA-CPSv4. The CMA-CPSv4 model code is based on BCC-CSM2-HR and the BCC-ESM1. The source code of the BCC-CSM2-HR model can be accessed at a DOI repository (https://doi.org/10.5281/zenodo.4127457; Wu et al., 2020a). The source code of BCC-ESM1 and model input files for CMA-CPSv4 can be accessed at a DOI repository (https://doi.org/10.5281/zenodo.3609337; Wu et al., 2020c). CMA-CPSv4 is the latest-generation operational climate prediction system of the China Meteorological Administration. Due to intellectual property copyright restrictions, we cannot provide the source code for CMA-CPSv4, but a copy can be made available to the reviewers of this work. All source code and data can also be accessed by contacting the corresponding author Tongwen Wu (twwu@cma.gov.cn).

Data availability. MERRA-2 reanalysis can be obtained from the NASA Goddard Earth Sciences Data and Information Services Centre (GES DISC; https://disc.gsfc.nasa.gov/datasets?project=MERRA-2, last access: 2 March 2025). Model output data from the 10 CMIP6 AerChemMIP simulations used in this paper are available from the Earth System Grid Federation (ESGF) (https://esgf-node.ornl.gov/search?project=input4MIPs, last access: 2 March 2025). Monthly average surface $PM_{2.5}$ observations in East Asia are available from the Acid Deposition Monitoring Network in East Asia (EANET, http://www.eanet.asia, last access: 4 March 2025, Ohizumi, 2023) and the Chinese National Environmental Monitoring Center (CNEMC, http://www.cnemc.cn, last access: 6 March 2025). Biomass burning emissions (Van Marle et al., 2017) and anthropogenic and open burning emissions (Feng et al., 2020; Gidden et al., 2019; Hoesly et al., 2018) are obtained from the ESGF (https://esgf-node.llnl.gov/search/input4mips/, last access: 4 January 2025). The AERONET data are downloaded at https://aeronet.gsfc.nasa.gov/new_web/ (last accessed: 18 March 2025; Holben et al., 1998). MODIS data are available at https://ladsweb.modaps.eosdis.nasa.gov/ (last accessed: 20 March 2025, Platnick et al., 2017); MISR data can be downloaded via https://l0dup05.larc.nasa.gov/L3Web/ (last accessed: 20 March 2025, Diner et al., 1998). ERA5 reanalysis data (Hersbach et al., 2020) are available from the Copernicus Climate Change Service (https://doi.org/10.24381/cds.4991cf48, Hersbach et al., 2023a; https://doi.org/10.24381/cds.50314f4c, Hersbach et al., 2023b). The HTAP_v3 region definitions are available here: https://zenodo.org/records/12654038 (last access: 20 March 2025, Butler, 2024). The simulation outputs of CMA-CPSv4 in this study are available at https://zenodo.org/records/18465065 (last access: 3 February 2026, Zheng et al., 2026).

Author contributions. TW designed the experiments, and MZ carried them out. The first draft of the manuscript was written by MZ and all authors commented on previous versions of the manuscript. All authors discussed the results and approved the final manuscript.

Competing interests. The contact author has declared that none of the authors has any competing interests.

Acknowledgements. The CMA-CPSv4 project is supported by the Earth System Numerical Prediction Centre of the China Meteorological Administration. We acknowledge the China Meteorological Administration's High-Performance Computing Public Service Platform.

Financial support. This work was supported by National Natural Science Foundation of China (Grant No. 42230608).

Review statement. This paper was edited by Samuel Remy and reviewed by two anonymous referees.

References

Albrecht, B. A.: Aerosols, cloud microphysics, and fractional cloudiness, Science, 245, 1227–1230, https://doi.org/10.1126/science.245.4923.1227, 1989.

Ångström, A.: On the atmospheric transmission of sun radiation and on dust in the air, Geogr. Ann., 11, 156–166, https://doi.org/10.2307/519399, 1929.

Asaadi, A., Schwinger, J., Lee, H., Tjiputra, J., Arora, V., Séférian, R., Liddicoat, S., Hajima, T., Santana-Falcón, Y., and Jones, C. D.: Carbon cycle feedbacks in an idealized simulation and a scenario simulation of negative emissions in CMIP6 Earth system models, Biogeosciences, 21, 411–435, https://doi.org/10.5194/bg-21-411-2024, 2024.

Bathiany, S., Claussen, M., Brovkin, V., Raddatz, T., and Gayler, V.: Combined biogeophysical and biogeochemical effects of large-scale forest cover changes in the MPI earth system model, Biogeosciences, 7, 1383–1399, https://doi.org/10.5194/bg-7-1383-2010, 2010.

Benedetti, A. and Vitart, F.: Can the direct effect of aerosols improve subseasonal predictability?, Mon. Weather Rev., 146, 3481–3498, https://doi.org/10.1175/MWR-D-17-0282.1, 2018.

Bhattacharjee, P., Zhang, L., Baker, B., Pan, L., Montuoro, R., Grell, G., and McQueen, J.: Evaluation of Aerosol Optical Depth Forecasts from NOAA's Global Aerosol Forecast Model (GEFS-Aerosols), Wea. Forecasting, 38, 225–249, https://doi.org/10.1175/WAF-D-22-0083.1, 2023.

Bodas-Salcedo, A., Ringer, M. A., and Jones, A.: Evaluation of the Surface Radiation Budget in the Atmospheric Component of the Hadley Centre Global Environmental Model (HadGEM1), J. Climate, 21, 4723–4748, https://doi.org/10.1175/2008JCLI2097.1, 2008.

Boucher, O. and Lohmann, U.: The sulphate-CCN-cloud albedo effect – a sensitivity study with two general circulation models, Tellus B, 47, 281–300, https://doi.org/10.3402/tellusb.v47i3.16048, 1995

Buchard, V., Randles, C. A., Da Silva, A. M., Darmenov, A., Colarco, P. R., Govindaraju, R., Ferrare, R., Hair, J., Beyersdorf, A. J., and Ziemba, L. D.: The MERRA-2 aerosol reanalysis, 1980 onward, Part II: Evaluation and case studies, J. Climate, 30, 6851–6872, https://doi.org/10.1175/JCLI-D-16-0613.1, 2017.

Butler, T: Source region definitions for the HTAP3-OPNS multi-model exercise, Zenodo [data set], https://doi.org/10.5281/zenodo.12654038, 2024

Chylek, P., Li, J., Dubey, M. K., Wang, M., and Lesins, G.: Observed and model simulated 20th century Arctic temperature variability: Canadian Earth System Model

CanESM2, Atmos. Chem. Phys. Discuss., 11, 22893–22907, https://doi.org/10.5194/acpd-11-22893-2011, 2011.

Collins, W. J., Lamarque, J.-F., Schulz, M., Boucher, O., Eyring, V., Hegglin, M. I., Maycock, A., Myhre, G., Prather, M., and Shindell, D.: AerChemMIP: Quantifying the effects of chemistry and aerosols in CMIP6, Geosci. Model Dev., 10, 585–607, https://doi.org/10.1007/s00376-020-0151-2, 2017.

Crippa, M., Guizzardi, D., Butler, T., Keating, T., Wu, R., Kaminski, J., Kuenen, J., Kurokawa, J., Chatani, S., Morikawa, T., Pouliot, G., Racine, J., Moran, M. D., Klimont, Z., Manseau, P. M., Mashayekhi, R., Henderson, B. H., Smith, S. J., Suchyta, H., Muntean, M., Solazzo, E., Banja, M., Schaaf, E., Pagani, F., Woo, J.-H., Kim, J., Monforti-Ferrario, F., Pisoni, E., Zhang, J., Niemi, D., Sassi, M., Ansari, T., and Foley, K.: The HTAP_v3 emission mosaic: merging regional and global monthly emissions (2000–2018) to support air quality modelling and policies, Earth Syst. Sci. Data, 15, 2667–2694, https://doi.org/10.5194/essd-15-2667-2023, 2023.

Dai, T., Goto, D., Schutgens, N. A. J., Dong, X., Shi, G., and Nakajima, T.: Simulated aerosol key optical properties over global scale using an aerosol transport model coupled with a new type of dynamic core, Atmos. Environ., 82, 71–82, https://doi.org/10.1016/j.atmosenv.2013.10.018, 2014.

Delworth, T. L., Broccoli, A. J., Rosati, A., Stouffer, R. J., Balaji, V., Beesley, J. A., Cooke, W. F., Dixon, K. W., Dunne, J., Dunne, K. A., Durachta, J. W., Findell, K. L., Ginoux, P., Gnanadesikan, A., Gordon, C. T., Griffies, S. M., Gudgel, R., Harrison, M. J., Held, I. M., Hemler, R. S., Horowitz, L. W., Klein, S. A., Knutson, T. R., Kushner, P. J., Langenhorst, A. R., Lee, H.-C., Lin, S.-J., Lu, J., Malyshev, S. L., Milly, P. C. D., Ramaswamy, V., Russell, J., Schwarzkopf, M. D., Shevliakova, E., Sirutis, J. J., Spelman, M. J., Stern, W. F., Winton, M., Wittenberg, A. T., Wyman, B., Zeng, F., and Zhang, R.: GFDL's CM2 Global Coupled Climate Models, Part I: Formulation and Simulation Characteristics, J. Climate, 19, 643–674, https://doi.org/10.1175/JCLI3629.1, 2006.

Diner, D. J., Beckert, J. C., Reilly, T. H., Bruegge, C. J., Conel, J. E., Kahn, R. A., Martonchik, J. V., Ackerman, T. P., Davies, R., Gerstl, S. A. W., Gordon, H. R., Muller, J.-P., Myneni, R. B., Sellers, P. J., Pinty, B., and Verstraete, M. M.: Multi-angle Imaging SpectroRadiometer (MISR) instrument description and experiment overview, IEEE Trans. Geosci. Remote Sens., 36, 1072–1087, https://doi.org/10.1109/36.700992, 1998.

Dunne, J. P., Horowitz, L. W., Adcroft, A. J., Ginoux, P., Held, I. M., John, J. G., Krasting, J. P., Malyshev, S., Naik, V., Paulot, F., Shevliakova, E., Stock, C. A., Zadeh, N., Balaji, V., Blanton, C., Dunne, K. A., Dupuis, C., Durachta, J., Dussin, R., Gauthier, P. P. G., Griffies, S. M., Guo, H., Hallberg, R. W., Harrison, M., He, J., Hurlin, W., McHugh, C., Menzel, R., Milly, P. C. D., Nikonov, S., Paynter, D. J., Ploshay, J., Radhakrishnan, A., Rand, K., Reichl, B. G., Robinson, T., Schwarzkopf, D. M., Sentman, L. T., Underwood, S., Vahlenkamp, H., Winton, M., Wittenberg, A. T., Wyman, B., Zeng, Y., and Zhao, M.: The GFDL Earth System Model Version 4.1 (GFDL-ESM 4.1): Overall Coupled Model Description and Simulation Characteristics, J. Adv. Model. Earth Syst., 12, e2019MS002015, https://doi.org/10.1029/2019MS002015, 2020.

Eyring, V., Bony, S., Meehl, G. A., Senior, C. A., Stevens, B., Stouffer, R. J., and Taylor, K. E.: Overview of the Coupled Model Intercomparison Project Phase 6 (CMIP6) experimental design and organization, Geosci. Model Dev., 9, 1937–1958, https://doi.org/10.5194/gmd-9-1937-2016, 2016.

Feng, L., Smith, S. J., Braun, C., Crippa, M., Gidden, M. J., Hoesly, R., Klimont, Z., van Marle, M., van den Berg, M., and van der Werf, G. R.: The generation of gridded emissions data for CMIP6, Geosci. Model Dev., 13, 461–482, https://doi.org/10.5194/gmd-13-461-2020, 2020.

Firpo, M. Â. F., Guimarães, B. dos S., Dantas, L. G., Silva, M. G. B. da, Alves, L. M., Chadwick, R., Llopart, M. P., and de Oliveira, G. S.: Assessment of CMIP6 models' performance in simulating present-day climate in Brazil, Front. Clim., 4, https://doi.org/10.3389/fclim.2022.948499, 2022.

Flato, G. M.: Earth system models: an overview, WIREs Climate Change, 2, 783–800, https://doi.org/10.1002/wcc.148, 2011.

Fletcher, C. G., Kravitz, B., and Badawy, B.: Quantifying uncertainty from aerosol and atmospheric parameters and their impact on climate sensitivity, Atmos. Chem. Phys., 18, 17529–17543, https://doi.org/10.5194/acp-18-17529-2018, 2018.

Friedlingstein, P., Cox, P., Betts, R., Bopp, L., Bloh, W. von, Brovkin, V., Cadule, P., Doney, S., Eby, M., Fung, I., Bala, G., John, J., Jones, C., Joos, F., Kato, T., Kawamiya, M., Knorr, W., Lindsay, K., Matthews, H. D., Raddatz, T., Rayner, P., Reick, C., Roeckner, E., Schnitzler, K.-G., Schnur, R., Strassmann, K., Weaver, A. J., Yoshikawa, C., and Zeng, N.: Climate–Carbon Cycle Feedback Analysis: Results from the C4MIP Model Intercomparison, J. Climate, 19, 3337–3353, https://doi.org/10.1175/JCLI3800.1, 2006.

Friedlingstein, P., Meinshausen, M., Arora, V. K., Jones, C. D., Anav, A., Liddicoat, S. K., and Knutti, R.: Uncertainties in CMIP5 Climate Projections due to Carbon Cycle Feedbacks, J. Climate, 27, 511–526, https://doi.org/10.1175/JCLI-D-12-00579.1, 2014.

Gelaro, R., McCarty, W., Suárez, M. J., Todling, R., Molod, A., Takacs, L., Randles, C. A., Darmenov, A., Bosilovich, M. G., and Reichle, R.: The modern-era retrospective analysis for research and applications, version 2 (MERRA-2), J. Climate, 30, 5419–5454, https://doi.org/10.1175/JCLI-D-16-0758.1, 2017.

Gidden, M. J., Riahi, K., Smith, S. J., Fujimori, S., Luderer, G., Kriegler, E., van Vuuren, D. P., van den Berg, M., Feng, L., Klein, D., Calvin, K., Doelman, J. C., Frank, S., Fricko, O., Harmsen, M., Hasegawa, T., Havlik, P., Hilaire, J., Hoesly, R., Horing, J., Popp, A., Stehfest, E., and Takahashi, K.: Global emissions pathways under different socioeconomic scenarios for use in CMIP6: a dataset of harmonized emissions trajectories through the end of the century, Geosci. Model Dev., 12, 1443–1475, https://doi.org/10.5194/gmd-12-1443-2019, 2019.

Ginoux, P., Prospero, J. M., Gill, T. E., Hsu, N. C., and Zhao, M.: Global-scale attribution of anthropogenic and natural dust sources and their emission rates based on MODIS Deep Blue aerosol products, Rev. Geophys., 50, https://doi.org/10.1029/2012RG000388, 2012.

Griffies, S. M.: Elements of the Modular Ocean Model (MOM), GFDL Ocean Group Technical Report No. 7, NOAA/Geophysical Fluid Dynamics Laboratory, 632 + xiii pages, https://mom-ocean.github.io/assets/pdfs/MOM5_manual.pdf (last access: 6 March 2025), 2012

Gui, K., Zhang, X., Che, H., Li, L., Zheng, Y., An, L., Miao, Y., Zhao, H., Dubovik, O., Holben, B., Wang, J., Gupta, P., Lind, E. S., Toledano, C., Wang, H., Wang, Z., Wang, Y., Huang, X., Dai, K., Xia, X., Xu, X., and Zhang, X.: Advancing operational global aerosol forecasting with machine learning, Nature, 651, 658–665, https://doi.org/10.1038/s41586-026-10234-y, 2026.

Hersbach, H., Bell, B., Berrisford, P., Hirahara, S., Horányi, A., Muñoz Sabater, J., Nicolas, J., Peubey, C., Radu, R., Schepers, D., Simmons, A., Soci, C., Abdalla, S., Abellan, X., Balsamo, G., Bechtold, P., Biavati, G., Bidlot, J., Bonavita, M., De Chiara, G., Dahlgren, P., Dee, D., Diamantakis, M., Dragani, R., Flemming, J., Forbes, R., Fuentes, M., Geer, A., Haimberger, L., Healy, S., Hogan, R. J., Hólm, E., Janisková, M., Keeley, S., Laloyaux, P., Lopez, P., Lupu, C., Radnoti, G., de Rosnay, P., Rozum, I., Vamborg, F., Villaume, S., and Thépaut, J.-N.: The ERA5 global reanalysis, Q. J. Roy. Meteor. Soc., 146, 1999–2049, https://doi.org/10.1002/qj.3803, 2020.

Hersbach, H., Comyn-Platt, E., Bell, B., Berrisford, P., Biavati, G., Horányi, A., Muñoz Sabater, J., Nicolas, J., Peubey, C., Radu, R., Rozum, I., Schepers, D., Simmons, A., Soci, C., Dee, D., Thépaut, J-N., Cagnazo, C., and Cucchi, M.: ERA5 post-processed daily statistics on single levels from 1940 to present, Climate Data Store [data set], https://doi.org/10.24381/cds.4991cf48, 2023a

Hersbach, H., Comyn-Platt, E., Bell, B., Berrisford, P., Biavati, G., Horányi, A., Muñoz Sabater, J., Nicolas, J., Peubey, C., Radu, R., Rozum, I., Schepers, D., Simmons, A., Soci, C., Dee, D., Thépaut, J-N., Cagnazo, C., and Cucchi, M.: ERA5 post-processed daily-statistics on pressure levels from 1940 to present, Climate Data Store [data set], https://doi.org/10.24381/cds.50314f4c, 2023b.

Hoesly, R. M., Smith, S. J., Feng, L., Klimont, Z., Janssens-Maenhout, G., Pitkanen, T., Seibert, J. J., Vu, L., Andres, R. J., Bolt, R. M., Bond, T. C., Dawidowski, L., Kholod, N., Kurokawa, J.-I., Li, M., Liu, L., Lu, Z., Moura, M. C. P., O'Rourke, P. R., and Zhang, Q.: Historical (1750–2014) anthropogenic emissions of reactive gases and aerosols from the Community Emissions Data System (CEDS), Geosci. Model Dev., 11, 369–408, https://doi.org/10.5194/gmd-11-369-2018, 2018.

Holben, B. N., Eck, T. F., Slutsker, I., Tanré, D., Buis, J. P., Setzer, A., Vermote, E., Reagan, J. A., Kaufman, Y. J., Nakajima, T., Lavenu, F., Jankowiak, I., and Smirnov, A.: AERONET – A Federated Instrument Network and Data Archive for Aerosol Characterization, Remote Sens. Environ., 66, 1–16, https://doi.org/10.1016/S0034-4257(98)00031-5, 1998.

Houghton, J. T., Ding, Y., Griggs, D. J., Noguer, M., van der Linden, P. J., Dai, X., Maskell, K., and Johnson, C. A.: Climate Change 2001: the Scientific Basis: Contribution of Working Group I to the Third Assessment Report of the Intergovernmental Panel on Climate Change, Cambridge University Press, ISBN 0-521-80767-0, 2001.

Huang, X. and Ding, A.: Aerosol as a critical factor causing forecast biases of air temperature in global numerical weather prediction models, Sci. Bull., 66, 1917–1924, https://doi.org/10.1016/j.scib.2021.05.009, 2021.

Jones, C. D., Arora, V., Friedlingstein, P., Bopp, L., Brovkin, V., Dunne, J., Graven, H., Hoffman, F., Ilyina, T., John, J. G., Jung, M., Kawamiya, M., Koven, C., Pongratz, J., Raddatz, T., Randerson, J. T., and Zaehle, S.: C4MIP – The Coupled Climate–Carbon Cycle Model Intercomparison Project: experimental protocol for CMIP6, Geosci. Model Dev., 9, 2853–2880, https://doi.org/10.5194/gmd-9-2853-2016, 2016.

Kahn, R., Banerjee, P., McDonald, D., and Diner, D. J.: Sensitivity of multiangle imaging to aerosol optical depth and to pure-particle size distribution and composition over ocean, J. Geophys. Res. Atmos., 103, 32195–32213, https://doi.org/10.1029/98JD01752, 1998.

Kaufhold, C., Willeit, M., Talento, S., Ganopolski, A., and Rockström, J.: Interplay between climate and carbon cycle feedbacks could substantially enhance future warming, Environ. Res. Lett., 20, 044027, https://doi.org/10.1088/1748-9326/adb6be, 2025.

Keller, C. A., Knowland, K. E., Duncan, B. N., Liu, J., Anderson, D. C., Das, S., Lucchesi, R. A., Lundgren, E. W., Nicely, J. M., Nielsen, E., Ott, L. E., Saunders, E., Strode, S. A., Wales, P. A., Jacob, D. J., and Pawson, S.: Description of the NASA GEOS Composition Forecast Modeling System GEOS-CF v1.0, J. Adv. Model. Earth Syst., 13, e2020MS002413, https://doi.org/10.1029/2020MS002413, 2021.

Kong, S. S.-K., Fu, J. S., Lin, N.-H., Sheu, G.-R., and Huang, W.-S.: Modeling CMAQ dry deposition treatment over the western Pacific: a distinct characteristic of mineral dust and anthropogenic aerosols, Atmos. Chem. Phys., 25, 7245–7268, https://doi.org/10.5194/acp-25-7245-2025, 2025.

Lamarque, J.-F., Emmons, L. K., Hess, P. G., Kinnison, D. E., Tilmes, S., Vitt, F., Heald, C. L., Holland, E. A., Lauritzen, P. H., Neu, J., Orlando, J. J., Rasch, P. J., and Tyndall, G. K.: CAM-chem: description and evaluation of interactive atmospheric chemistry in the Community Earth System Model, Geosci. Model Dev., 5, 369–411, https://doi.org/10.5194/gmd-5-369-2012, 2012.

Li, W., Zhang, Y., Shi, X., Zhou, W., Huang, A., Mu, M., Qiu, B., and Ji, J.: Development of land surface model BCC_AVIM2.0 and its preliminary performance in LS3MIP/CMIP6, J. Meteorol. Res., 33, 851–869, https://doi.org/10.1007/s13351-019-9016-y, 2019.

Liang, X., Li, Q., and Wu, T.: Dynamical seasonal prediction of the asian summer monsoon in the China meteorological administration climate prediction system version 3, Front. Earth Sci., 10, 934248, https://doi.org/10.3389/feart.2022.934248, 2022.

Liu, X., Yao, J., Wu, T., Zhang, S., Xu, F., Zhang, L., Jie, W., Zhou, W., Li, Q., Liang, X., Chu, M., Yan, J., Nie, S., and Cheng, Y.: Development of Coupled Data Assimilation With the BCC Climate System Model: Highlighting the Role of Sea-Ice Assimilation for Global Analysis, J. Adv. Model. Earth Syst., 13, e2020MS002368, https://doi.org/10.1029/2020MS002368, 2021.

Liu, Y.-W., Zhao, L., Tan, G.-R., Shen, X.-Y., Nie, S.-P., Li, Q.-Q., and Zhang, L.: Evaluation of multidimensional simulations of summer air temperature in China from CMIP5 to CMIP6 by the BCC models: From trends to modes, Adv. Clim. Change Res., 13, 28–41, https://doi.org/10.1016/j.accre.2021.12.001, 2022.

Lohmann, U. and Ferrachat, S.: Impact of parametric uncertainties on the present-day climate and on the anthropogenic aerosol effect, Atmos. Chem. Phys., 10, 11373–11383, https://doi.org/10.5194/acp-10-11373-2010, 2010a.

Lohmann, U., Rotstayn, L., Storelvmo, T., Jones, A., Menon, S., Quaas, J., Ekman, A. M. L., Koch, D., and Ruedy, R.: Total aerosol effect: radiative forcing or radiative flux perturbation?, Atmos. Chem. Phys., 10, 3235–3246, https://doi.org/10.5194/acp-10-3235-2010, 2010b.

Lu, Y., Wu, T., Jie, W., Scaife, A. A., Andrews, M. B., and Richter, J. H.: Variability of the Stratospheric Quasi-Biennial Oscillation and Its Wave Forcing Simulated in the Beijing Climate Center Atmospheric General Circulation Model, J. Atmos. Sci., 77, 149-165, https://doi.org/10.1175/JAS-D-19-0123.1, 2020.

Lu, Y., Wu, T., Li, Y., and Yang, B.: Mitigation of the double ITCZ syndrome in BCC-CSM2-MR through improving parameterizations of boundary-layer turbulence and shallow convection, Geosci. Model Dev., 14, 5183–5204, https://doi.org/10.5194/gmd-14-5183-2021, 2021.

Lu, Y., Jin, L., Zhong, J., Zhang, X., Zhang, Y., Wu, F., Zhang, F., Wang, Z., Zhang, J., Xin, X., Wu, T., Wang, D., Zhang, D., Tianpeng, W., and Hua, W.: Earth system responses under a global 2 °C-target scenario aligned with China's carbon neutrality pledge, Environ. Res. Lett., 20, 104049, https://doi.org/10.1088/1748-9326/adfbfb, 2025.

Mahowald, N., Lamarque, J.-F., Tie, X., and Wolff, E.: Sea salt aerosol response to climate change: last glacial maximum, preindustrial and doubled carbon dioxide climates, J. Geophys. Res., 111, D05303, https://doi.org/10.1029/2005JD006459, 2006.

McCormick, R. A. and Ludwig, J. H.: Climate modification by atmospheric aerosols, Science, 156, 1358–1359, https://doi.org/10.1126/science.156.3780.1358, 1967.

Ming, Y., Ramaswamy, V., Ginoux, P. A., and Horowitz, L. H.: Direct radiative forcing of anthropogenic organic aerosol, J. Geophys. Res. Atmos., 110, https://doi.org/10.1029/2004JD005573, 2005.

Molod, A., Hackert, E., Vikhliaev, Y., Zhao, B., Barahona, D., Vernieres, G., Borovikov, A., Kovach, R. M., Marshak, J., Schubert, S., Li, Z., Lim, Y.-K., Andrews, L. C., Cullather, R., Koster, R., Achuthavarier, D., Carton, J., Coy, L., Friere, J. L. M., Longo, K. M., Nakada, K., and Pawson, S.: GEOS-S2S Version 2: The GMAO High-Resolution Coupled Model and Assimilation System for Seasonal Prediction, J. Geophys. Res. Atmos., 125, e2019JD031767, https://doi.org/10.1029/2019JD031767, 2020.

Mulcahy, J. P., Walters, D. N., Bellouin, N., and Milton, S. F.: Impacts of increasing the aerosol complexity in the Met Office global numerical weather prediction model, Atmos. Chem. Phys., 14, 4749–4778, https://doi.org/10.5194/acp-14-4749-2014, 2014.

Ohizumi, T.: Acid Deposition Monitoring Network in East Asia (EANET), Springer Nature Singapore, 157–166, https://doi.org/10.1007/978-981-15-2760-9_11, 2023.

Platnick, S., King, M., and Hubanks, P.: MODIS Atmosphere L3 Monthly Product, NASA MODIS Adaptive Processing System, Goddard Space Flight Center, LAADS DAAC [data set], https://doi.org/10.5067/MODIS/MOD08_M3.061, 2017.

Pleim, J. E., Ran, L., Saylor, R. D., Willison, J., and Binkowski, F. S.: A New Aerosol Dry Deposition Model for Air Quality and Climate Modeling, J. Adv. Model. Earth Syst., 14, e2022MS003050, https://doi.org/10.1029/2022MS003050, 2022.

Provençal, S., Buchard, V., da Silva, A. M., Leduc, R., Barrette, N., Elhacham, E., and Wang, S.-H.: Evaluation of PM2.5 surface concentration simulated by Version 1 of the NASA's MERRA Aerosol Reanalysis over Israel and Taiwan, Aerosol Air Qual. Res., 17, 253–261, https://doi.org/10.4209/aaqr.2016.04.0145, 2017.

Quaas, J., Boucher, O., and Lohmann, U.: Constraining the total aerosol indirect effect in the LMDZ and ECHAM4 GCMs using MODIS satellite data, Atmos. Chem. Phys., 6, 947–955, https://doi.org/10.5194/acp-6-947-2006, 2006.

Randles, C. A., Da Silva, A. M., Buchard, V., Colarco, P. R., Darmenov, A., Govindaraju, R., Smirnov, A., Holben, B., Ferrare, R., and Hair, J.: The MERRA-2 aerosol reanalysis, 1980 onward. Part I: System description and data assimilation evaluation, J. Climate, 30, 6823–6850, https://doi.org/10.1175/JCLI-D-16-0609.1, 2017.

Rémy, S., Kipling, Z., Huijnen, V., Flemming, J., Nabat, P., Michou, M., Ades, M., Engelen, R., and Peuch, V.-H.: Description and evaluation of the tropospheric aerosol scheme in the Integrated Forecasting System (IFS-AER, cycle 47R1) of ECMWF, Geosci. Model Dev., 15, 4881–4912, https://doi.org/10.5194/gmd-15-4881-2022, 2022.

Ren, F., Lin, J., Xu, C., Adeniran, J. A., Wang, J., Martin, R. V., van Donkelaar, A., Hammer, M. S., Horowitz, L. W., Turnock, S. T., Oshima, N., Zhang, J., Bauer, S., Tsigaridis, K., Seland, Ø., Nabat, P., Neubauer, D., Strand, G., van Noije, T., Le Sager, P., and Takemura, T.: Evaluation of CMIP6 model simulations of $PM_{2.5}$ and its components over China, Geosci. Model Dev., 17, 4821–4836, https://doi.org/10.5194/gmd-17-4821-2024, 2024.

Rosenfeld, D.: Suppression of Rain and Snow by Urban and Industrial Air Pollution, Science, 287, 1793–1796, https://doi.org/10.1126/science.287.5459.1793, 2000.

Schuster, G. L., Dubovik, O., and Holben, B. N.: Angstrom exponent and bimodal aerosol size distributions, J. Geophys. Res. Atmos., 111, https://doi.org/10.1029/2005jd006328, 2006.

Sellar, A. A., Jones, C. G., Mulcahy, J. P., Tang, Y., Yool, A., Wiltshire, A., O'connor, F. M., Stringer, M., Hill, R., and Palmieri, J.: UKESM1: Description and evaluation of the UK Earth System Model, J. Adv. Model. Earth Syst., 11, 4513–4558, https://doi.org/10.1029/2019MS001739, 2019.

Shrivastava, M., Cappa, C. D., Fan, J., Goldstein, A. H., Guenther, A. B., Jimenez, J. L., Kuang, C., Laskin, A., Martin, S. T., Ng, N. L., Petaja, T., Pierce, J. R., Rasch, P. J., Roldin, P., Seinfeld, J. H., Shilling, J., Smith, J. N., Thornton, J. A., Volkamer, R., Wang, J., Worsnop, D. R., Zaveri, R. A., Zelenyuk, A., and Zhang, Q.: Recent advances in understanding secondary organic aerosol: Implications for global climate forcing, Rev. Geophys., 55, 509–559, https://doi.org/10.1002/2016RG000540, 2017.

Silva, R. A., West, J. J., Lamarque, J.-F., Shindell, D. T., Collins, W. J., Faluvegi, G., Folberth, G. A., Horowitz, L. W., Nagashima, T., Naik, V., Rumbold, S. T., Sudo, K., Takemura, T., Bergmann, D., Cameron-Smith, P., Doherty, R. M., Josse, B., MacKenzie, I. A., Stevenson, D. S., and Zeng, G.: Future global mortality from changes in air pollution attributable to climate change, Nat. Clim. Change, 7, 647–651, https://doi.org/10.1038/nclimate3354, 2017.

Su, X., Wu, T., Zhang, J., Zhang, Y., Jin, J., Zhou, Q., Zhang, F., Liu, Y., Zhou, Y., Zhang, L., Turnock, S. T., and Furtado, K.: Present-Day PM2.5 over Asia: Simulation and Uncertainty in CMIP6 ESMs, J. Meteorol. Res., 36, 429–449, https://doi.org/10.1007/s13351-022-1202-7, 2022.

Sun, S., Grell, G. A., Zhang, L., Henderson, J. K., Wang, S., Heinzeller, D., Li, H., Meixner, J., and Bhattacharjee, P. S.: Simulating the effects of aerosol-radiation interactions on subseasonal prediction using the coupled Unified Forecast System and CCPP-

Chem: Interactive aerosol module versus prescribed aerosol climatology, J. Adv. Model. Earth Syst., 17, e2024MS004392, https://doi.org/10.1029/2024MS004392, 2025.

Taylor, K. E., Stouffer, R. J., and Meehl, G. A.: An overview of CMIP5 and the experiment design, B. Am. Meteorol. Soc., 93, 485–498, 2012.

Tilmes, S., Lamarque, J.-F., Emmons, L. K., Kinnison, D. E., Ma, P.-L., Liu, X., Ghan, S., Bardeen, C., Arnold, S., Deeter, M., Vitt, F., Ryerson, T., Elkins, J. W., Moore, F., Spackman, J. R., and Val Martin, M.: Description and evaluation of tropospheric chemistry and aerosols in the Community Earth System Model (CESM1.2), Geosci. Model Dev., 8, 1395–1426, https://doi.org/10.5194/gmd-8-1395-2015, 2015.

Turnock, S. T., Allen, R. J., Andrews, M., Bauer, S. E., Deushi, M., Emmons, L., Good, P., Horowitz, L., John, J. G., Michou, M., Nabat, P., Naik, V., Neubauer, D., O'Connor, F. M., Olivié, D., Oshima, N., Schulz, M., Sellar, A., Shim, S., Takemura, T., Tilmes, S., Tsigaridis, K., Wu, T., and Zhang, J.: Historical and future changes in air pollutants from CMIP6 models, Atmos. Chem. Phys., 20, 14547–14579, https://doi.org/10.5194/acp-20-14547-2020, 2020.

Twomey, S.: Pollution and the planetary albedo, Atmos. Environ., 8, 1251–1256, https://doi.org/10.1016/0004-6981(74)90004-3, 1974.

Twomey, S.: The Influence of Pollution on the Shortwave Albedo of Clouds, J. Atmos. Sci., 34, 1149–1152, https://doi.org/10.1175/1520-0469(1977)034<1149:TIOPOT>2.0.CO;2, 1977.

Van Marle, M. J. E., Kloster, S., Magi, B. I., Marlon, J. R., Daniau, A.-L., Field, R. D., Arneth, A., Forrest, M., Hantson, S., Kehrwald, N. M., Knorr, W., Lasslop, G., Li, F., Mangeon, S., Yue, C., Kaiser, J. W., and van der Werf, G. R.: Historic global biomass burning emissions for CMIP6 (BB4CMIP) based on merging satellite observations with proxies and fire models (1750–2015), Geosci. Model Dev., 10, 3329–3357, https://doi.org/10.5194/gmd-10-3329-2017, 2017.

Van Noije, T., Bergman, T., Le Sager, P., O'Donnell, D., Makkonen, R., Gonçalves-Ageitos, M., Döscher, R., Fladrich, U., von Hardenberg, J., Keskinen, J.-P., Korhonen, H., Laakso, A., Myriokefalitakis, S., Ollinaho, P., Pérez García-Pando, C., Reerink, T., Schrödner, R., Wyser, K., and Yang, S.: EC-Earth3-AerChem: a global climate model with interactive aerosols and atmospheric chemistry participating in CMIP6 , Geosci. Model Dev., 14, 5637–5668, https://doi.org/10.5194/gmd-14-5637-2021, 2021.

Watanabe, S., Hajima, T., Sudo, K., Nagashima, T., Takemura, T., Okajima, H., Nozawa, T., Kawase, H., Abe, M., Yokohata, T., Ise, T., Sato, H., Kato, E., Takata, K., Emori, S., and Kawamiya, M.: MIROC-ESM 2010: model description and basic results of CMIP5-20c3m experiments, Geosci. Model Dev., 4, 845–872, https://doi.org/10.5194/gmd-4-845-2011, 2011.

Wei, Y., Chen, X., Chen, H., Li, J., Wang, Z., Yang, W., Ge, B., Du, H., Hao, J., Wang, W., Li, J., Sun, Y., and Huang, H.: IAP-AACM v1.0: a global to regional evaluation of the atmospheric chemistry model in CAS-ESM, Atmos. Chem. Phys., 19, 8269–8296, https://doi.org/10.5194/acp-19-8269-2019, 2019.

Wu, T.: A mass-flux cumulus parameterization scheme for large-scale models: description and test with observations, Clim. Dyn., 38, 725–744, https://doi.org/10.1007/s00382-011-0995-3, 2012

Wu, T., Li, W., Ji, J., Xin, X., Li, L., Wang, Z., Zhang, Y., Li, J., Zhang, F., Wei, M., Shi, X., Wu, F., Zhang, L., Chu, M., Jie, W., Liu, Y., Wang, F., Liu, X., Li, Q., Dong, M., Liang, X., Gao, Y., and Zhang, J.: Global carbon budgets simulated by the Beijing Climate Center Climate System Model for the last century, J. Geophys. Res. Atmos., 118, 4326–4347, https://doi.org/10.1002/jgrd.50320, 2013.

Wu, T., Song, L., Li, W., Wang, Z., Zhang, H., Xin, X., Zhang, Y., Zhang, L., Li, J., Wu, F., Liu, Y., Zhang, F., Shi, X., Chu, M., Zhang, J., Fang, Y., Wang, F., Lu, Y., Liu, X., Wei, M., Liu, Q., Zhou, W., Dong, M., Zhao, Q., Ji, J., Li, L., and Zhou, M.: An overview of BCC climate system model development and application for climate change studies, J. Meteor. Res., 28, 34–56, https://doi.org/10.1007/s13351-014-3041-7, 2014.

Wu, T., Lu, Y., Fang, Y., Xin, X., Li, L., Li, W., Jie, W., Zhang, J., Liu, Y., Zhang, L., Zhang, F., Zhang, Y., Wu, F., Li, J., Chu, M., Wang, Z., Shi, X., Liu, X., Wei, M., Huang, A., Zhang, Y., and Liu, X.: The Beijing Climate Center Climate System Model (BCC-CSM): the main progress from CMIP5 to CMIP6 , Geosci. Model Dev., 12, 1573–1600, https://doi.org/10.5194/gmd-12-1573-2019, 2019.

Wu, T., Yu, R., Lu, Y., Jie, W., Fang, Y., Zhang, F., Zhang, J., Zhang, L., Xin, X., Wang, Z., Liu, Y., Wu, F., Chu, M., Li, J., Li, W., Zhang, Y., Shi, X., Yao, J., Liu, X., Yan, J., Zhao, H., Wei, M., Zhou, W., Li, L., Xue, W., Huang, A., Zhang, Y., Zhang, Y., and Shu, Q.: Source code for Wu et al., "BCC-CSM2-HR: A High-Resolution Version of the Beijing Climate Center Climate System Model", Geosci. Model Dev. publication, Zenodo [code], https://doi.org/10.5281/zenodo.4127457, 2020a.

Wu, T., Zhang, F., Zhang, J., Jie, W., Zhang, Y., Wu, F., Li, L., Yan, J., Liu, X., Lu, X., Tan, H., Zhang, L., Wang, J., and Hu, A.: Beijing Climate Center Earth System Model version 1 (BCC-ESM1): model description and evaluation of aerosol simulations, Geosci. Model Dev., 13, 977–1005, https://doi.org/10.5194/gmd-13-977-2020, 2020b.

Wu, T., Zhang, F., Zhang, J., Jie, W., Zhang, Y., Wu, F., Li, L., Yan, J., Liu, X., Lu, X., Tan, H., Zhang, L., Wang, J., and Hu, A.: Model code and data for Wu et al., "Beijing Climate Center Earth System Model version 1 (BCC-ESM1): Model Description and Evaluation of Aerosol Simulations", GMD publication, Zenodo [code and data set], https://doi.org/10.5281/zenodo.3609337, 2020c.

Wu, T., Yu, R., Lu, Y., Jie, W., Fang, Y., Zhang, J., Zhang, L., Xin, X., Li, L., Wang, Z., Liu, Y., Zhang, F., Wu, F., Chu, M., Li, J., Li, W., Zhang, Y., Shi, X., Zhou, W., Yao, J., Liu, X., Zhao, H., Yan, J., Wei, M., Xue, W., Huang, A., Zhang, Y., Zhang, Y., Shu, Q., and Hu, A.: BCC-CSM2-HR: a high-resolution version of the Beijing Climate Center Climate System Model, Geosci. Model Dev., 14, 2977–3006, https://doi.org/10.5194/gmd-14-2977-2021, 2021.

Yang, J., Zhai, P., Wu, T., Yan, J., Zhang, G., Pei, L., Yan, Y., Miao, S., and Li, Z.: Evaluation of High-Resolution Downscaling Predictions for the July 2023 Extreme Rainstorm in the Beijing-Tianjin-Hebei Region Based on CMA-CPSv3, Int. J. Climatol., e8879, https://doi.org/10.1002/joc.8879, 2025.

Zender, C., Bian, H., and Newman, D.: Mineral Dust Entrainment and Deposition (DEAD) model: Description and 1990s dust climatology, J. Geophys. Res., 108, 4416, https://doi.org/10.1029/2002JD002775, 2003.

Zhang, H., Zhang, M., Jin, J., Fei, K., Ji, D., Wu, C., Zhu, J., He, J., Chai, Z., and Xie, J.: Description and climate simulation performance of CAS-ESM version 2, J. Adv. Model. Earth Syst., 12, e2020MS002210, https://doi.org/10.1029/2020MS002210, 2020.

Zhang, J., Wu, T., Zhang, F., Furtado, K., Xin, X., Shi, X., Li, J., Chu, M., Zhang, L., and Liu, Q.: Bcc-esm1 model datasets for the cmip6 aerosol chemistry model intercomparison project (aerchemmip), Adv. Atmos. Sci., 38, 317–328, https://doi.org/10.1007/s00376-020-0151-2, 2021a.

Zhang, J., Furtado, K., Turnock, S. T., Mulcahy, J. P., Wilcox, L. J., Booth, B. B., Sexton, D., Wu, T., Zhang, F., and Liu, Q.: The role of anthropogenic aerosols in the anomalous cooling from 1960 to 1990 in the CMIP6 Earth system models, Atmos. Chem. Phys., 21, 18609–18627, https://doi.org/10.5194/acp-21-18609-2021, 2021b.

Zhang, K., O'Donnell, D., Kazil, J., Stier, P., Kinne, S., Lohmann, U., Ferrachat, S., Croft, B., Quaas, J., Wan, H., Rast, S., and Feichter, J.: The global aerosol-climate model ECHAM-HAM, version 2: sensitivity to improvements in process representations, Atmos. Chem. Phys., 12, 8911–8949, https://doi.org/10.5194/acp-12-8911-2012, 2012.

Zheng, B., Zhang, Q., Zhang, Y., He, K. B., Wang, K., Zheng, G. J., Duan, F. K., Ma, Y. L., and Kimoto, T.: Heterogeneous chemistry: a mechanism missing in current models to explain secondary inorganic aerosol formation during the January 2013 haze episode in North China, Atmos. Chem. Phys., 15, 2031–2049, https://doi.org/10.5194/acp-15-2031-2015, 2015.

Zheng, M., Wu, T., Xin, X., Liu, X., Lu, Y., Jie, W., Xie, C., and Zhou, Y.: Simulation of MJO with improved deep convection scheme in different resolutions of BCC-CSM2 models, Clim. Dyn., 62, 2161–2185, https://doi.org/10.1007/s00382-023-07015-y, 2024.

Zheng, M., Wu, T., Lu, Y., Jie, W., Liu, Y., Xin, X., Zhang, J., Zhao, H., Zhang, X., and Yang, J.: CMA-CPSv4 aerosol simulation output data for the period 2001–2020, Zenodo [data set], https://doi.org/10.5281/zenodo.18465065, 2026.

Zhou, Y., Wu, T., Zhang, J., Zhang, Y., Zhang, Y., Zhao, H., Jie, W., Zhou, Y., and Furtado, K.: Variation of Dust in Northern China and Its Reproduction in BCC-ESM1 since 1980, J. Meteorol. Res., 37, 617–631, https://doi.org/10.1007/s13351-023-2195-6, 2023.